Immunosuppression is a conserved driver of tuberculosis susceptibility

Dmitri I. Kotov[1,2]*, Ophelia V. Lee[1], Daisy X. Ji[3], David L. Jaye[4], Sara Suliman[5], Cem Gabay[6], Russell E. Vance[1,2,7]*

[1]Divison of Immunology and Molecular Medicine, [2]Howard Hughes Medical Institute, University of California, Berkeley; [3]Department of Microbiology, New York University Grossman School of Medicine; [4]Department of Pathology and Laboratory Medicine, Emory University; [5]Division of Experimental Medicine, Department of Medicine, University of California, San Francisco; [6]Division of Rheumatology, Department of Medicine, University Hospital of Geneva; [7]Lead contact: Russell E. Vance
*Correspondence: dkotov@berkeley.edu, rvance@berkeley.edu

Summary

Mycobacterium tuberculosis (*Mtb*) causes 1.6 million deaths a year[1]. However, no individual mouse model fully recapitulates the hallmarks of human tuberculosis disease. Here we report that a comparison across three different susceptible mouse models identifies *Mtb*-induced gene signatures that predict active TB disease in humans significantly better than a signature from the standard C57BL/6 mouse model. An increase in lung myeloid cells, including neutrophils, was conserved across the susceptible mouse models, mimicking the neutrophilic inflammation observed in humans[2,3]. Myeloid cells in the susceptible models and non-human primates exhibited high expression of immunosuppressive molecules including the IL-1 receptor antagonist, which inhibits IL-1 signaling. Prior reports have suggested that excessive IL-1 signaling impairs *Mtb* control[4–6]. By contrast, we found that enhancement of IL-1 signaling via deletion of IL-1 receptor antagonist promoted bacterial control in all three susceptible mouse models. IL-1 signaling enhanced cytokine production by lymphoid and stromal cells, suggesting a mechanism for IL-1 signaling in promoting *Mtb* control. Thus, we propose that myeloid cell expression of immunosuppressive molecules is a conserved mechanism exacerbating *Mtb* disease in mice, non-human primates, and humans.

Introduction

Mycobacterium tuberculosis (*Mtb*) causes ~10 million new cases of active disease and 1.6 million deaths per year, and is the leading cause of mortality from a bacterial pathogen[1]. Unfortunately, treatment consists of at least a 4-6 month regimen of antibiotics, and the only approved vaccine has little to no efficacy in adults[7]. A greater understanding of the infection is essential, but this depends on animal models that appropriately mimic *Mtb* pathogenesis in humans. While mouse models have led to key discoveries such as the critical role of IFNγ[8,9] and TNF[10] in *Mtb* control, mouse models have also been criticized for not recapitulating key aspects of human disease, such as structured granuloma formation[11,12]. Further hallmarks of human *Mtb* infection include expression of type I interferon (IFN) stimulated genes and neutrophilia[2] and the standard C57BL/6 (B6) mouse model only weakly exhibits these hallmarks[6,13–15]. We recently described *Sp140*$^{-/-}$ mice as an *Mtb*-susceptible mouse model that mimics the exacerbated type I IFN signature seen in humans[16]. Deletion of the gene encoding the type I IFN receptor (*Ifnar1*) rescues the hypersusceptibility of *Sp140*$^{-/-}$ mice, implying a causal role of type I IFNs in *Mtb* pathogenesis in this model[16,17]. Other *Mtb* susceptible mouse models have been described, such as *Nos2*$^{-/-}$ and *Acod1*$^{-/-}$ mice[18,19], though it remains unclear whether disease in these models is also driven by type I IFN signaling. We hypothesized that there may be conserved features underlying the susceptibility of diverse mouse models, and that these features may be preserved across susceptible mice, non-human primates, and humans.

Neutrophilic inflammation is a major feature associated with tuberculosis disease across *Sp140*$^{-/-}$, *Nos2*$^{-/-}$, *Acod1*$^{-/-}$ and other susceptible mouse models[6,17,19–22], as well as during non-human primate[23,24] and human *Mtb*[3,25]. Depletion of neutrophils enhances bacterial control in diverse *Mtb*-susceptible mouse models, including *Sp140*$^{-/-}$, *Nos2*$^{-/-}$, and *Acod1*$^{-/-}$ mice[6,17,19]. However, the precise role of neutrophils in driving disease is unclear. One widely held view is that neutrophilic inflammation creates a replicative niche for the bacteria, including possibly within neutrophils themselves[26]. Neutrophilic inflammation, perhaps associated with pervasive necrotic cell death, is also hypothesized to liberate or provide nutrients to replicating bacteria. The production of neutrophil extracellular traps (NETs) is also speculated to somehow promote bacterial replication[20,27]. A major pathway for recruiting neutrophils to sites of inflammation is IL-1 (comprising IL-1α and IL-1β) and IL-1 is expressed at high levels in *Mtb*-susceptible mice[5,28] and humans[29]. Excessive IL-1 has been proposed to enhance bacterial replication[4], particularly in *Nos2*$^{-/-}$ mice[5,6], though the underlying mechanisms remain uncertain. IL-1 clearly has protective functions as mice deficient in IL-1 signaling are highly susceptible to *Mtb* infection[21,30–34].

IL-1 signaling is repressed by a soluble receptor antagonist (IL-1Ra, encoded by the *Il1rn* gene). We previously reported that even heterozygous deficiency in *Il1rn* markedly enhances bacterial control in susceptible *Sst1*^{S} mice, implying that a lack of IL-1 signaling, rather than excessive IL-1 signaling, underlies the susceptibility of these mice. However, disease in *Sst1*^{S} mice may be a unique case since it is driven by an exacerbated type I IFN response, and *Il1rn* is an interferon-stimulated gene. Thus, it remains unclear whether impairment of IL-1 signaling by IL-1Ra plays a role in humans or other *Mtb*-susceptible mouse models, especially *Nos2*$^{-/-}$ and *Acod1*$^{-/-}$ mice, in which *Mtb* infection is characterized by high levels of IL-1.

Here, in an effort to determine whether there are any general mechanisms underlying *Mtb* susceptibility, we used single cell RNA sequencing (scRNA-seq) to profile and characterize three different *Mtb*-susceptible mouse strains (*Sp140*$^{-/-}$, *Nos2*$^{-/-}$, *Acod1*$^{-/-}$ mice). Unlike *Sp140*$^{-/-}$ mice, we found that *Nos2*$^{-/-}$ and *Acod1*$^{-/-}$ mice did not exhibit a strong type I IFN signature and were not rescued by *Ifnar1* deficiency. Despite this, a signature conserved across all three strains was identified that was characterized by myeloid cell expression of immunosuppressive genes such as *Il1rn*. This conserved *Mtb*-susceptible mouse signature predicted human TB progression better than a signature obtained from resistant B6 mice. Given the importance of IL-1 signaling for *Mtb* control, and the strong expression of IL-1Ra in myeloid cells, we tested how IL-1Ra contributes to *Mtb* susceptibility. Global deletion as well as macrophage-specific deletion of IL-1Ra rescued bacterial control in *Sp140*$^{-/-}$ mice, demonstrating a major role for myeloid cell expression of this immunosuppressive molecule in driving *Mtb* disease. This contribution was shared across the susceptible mouse models, as IL-1Ra deletion also enhanced bacterial control in *Nos2*$^{-/-}$ and *Acod1*$^{-/-}$ mice. Together, these data suggest that immunosuppression by myeloid cells is a conserved feature of *Mtb* susceptibility across mice and humans.

Results

Mtb-susceptible mice more accurately model human infection than B6 mice

Human *Mtb* infection presents as a highly diverse spectrum of diseased and non-diseased states. The best conserved hallmarks of active disease include induction of type I interferon (IFN) genes and a myeloid cell inflammatory response, especially by neutrophils[2]. We previously demonstrated that *Sp140*$^{-/-}$ mice exhibit both hallmarks, and that these hallmarks drive susceptibility in these mice[16,17]. Neutrophil trafficking to the lungs also promotes *Mtb* susceptibility in other mouse models[20,35–37], including *Nos2*$^{-/-}$ and *Acod1*$^{-/-}$ mice[6,19]. Therefore,

we sought to test whether *Nos2*$^{-/-}$ and *Acod1*$^{-/-}$ mice share other attributes of the susceptibility of *Sp140*$^{-/-}$ mice, including type I IFN-driven disease. As myeloid cells are the primary reservoir of *Mtb*, we used our previously described single cell RNA-sequencing (scRNA-seq) workflow[17] to profile myeloid cells in *Mtb*-infected and naïve *Nos2*$^{-/-}$ and *Acod1*$^{-/-}$ mice. Infection with a fluorescent (wasabi^{+}) *Mtb* strain allowed us to distinguish infected and bystander cells in infected mice. The resulting datasets were integrated with our previously published B6 and *Sp140*$^{-/-}$ myeloid cell datasets[17] using the R package Seurat[38] (**Fig. 1a**). As these are CITE-seq[39] datasets, mRNA and protein expression of lineage and activation markers were implemented for the annotation of cell clusters (**Supplementary Fig. 1**). Potential batch effects were assessed by comparing differentially expressed genes (>2-fold change in expression, adjusted p value < 0.05) between the *Sp140*$^{-/-}$, *Nos2*$^{-/-}$, and *Acod1*$^{-/-}$ mice and the wild-type B6 mice. Comparison of major myeloid cell populations in naïve lungs revealed that very few genes were differentially regulated in all three *Mtb* susceptible mouse models, suggesting a lack of any major batch effects in the integrated dataset (**Supplementary Fig. 2**). Analysis of the myeloid cell clusters within the integrated dataset showed that the dominant myeloid cell populations (monocytes, macrophages, and neutrophils) are present in each genotype, but the relative frequency of some cell types varies across experimental conditions. For example, *Mtb*-infection resulted in activation of the interstitial macrophages (IMs), driving them to adopt either a proinflammatory *Cxcl9*$^{+}$ or an alternative *Spp1*$^{+}$ activation state[40–42] (**Fig. 1a**).

Given that neutrophilia exhibited by *Mtb* susceptible mouse models is a hallmark of human *Mtb* disease progression[3], we hypothesized that susceptible mouse models might mimic at least some conserved hallmarks of active human disease, in which case they can be a useful tool to study *Mtb* pathogenesis. To test this hypothesis, we identified lung myeloid gene signatures consisting of genes induced at least 8-fold in *Mtb*-infected susceptible mice relative to naïve lungs (**Supplementary Table 1**). The ability of these genes to discriminate *Mtb* cases from healthy controls in the TANDEM cohort[43] was quantified by calculating the area under the curve (AUC) for receiver operating characteristic (ROC) curves, with values closer to 1 indicating better classifiers of human disease (**Fig. 1b**). While there was no major difference in the ability of the signatures derived from the three susceptible mouse models to discern human disease, all the susceptible models considerably out-performed B6 mice, suggesting the susceptible mouse models better recapitulate characteristics of human disease than B6 mice.

Next, we sought to better understand why the susceptible models were all able to discriminate between *Mtb* cases and healthy controls by assessing whether the type I IFN response present in humans[2] and *Sp140*$^{-/-}$ mice[16,17] was also present in *Nos2*$^{-/-}$ and *Acod1*$^{-/-}$ animals. Using our previously published gene signatures that distinguish between type I IFN and IFNγ signaling[17], we classified cells as responding to type I IFN and/or IFNγ in our myeloid scRNA-seq dataset. As expected, very few cells from naïve lungs were positive for either the type I or II IFN signature (**Fig. 1c**). Conversely, *Mtb*-infected cells from every genotype had strong IFNγ signaling, especially in monocytes and macrophages (**Fig. 1c, 1d**). However, the type I IFN response was unique to the *Sp140*$^{-/-}$ mice, with strong type I IFN signaling in the neutrophils and IMs of these mice.

We experimentally tested whether type I IFN signaling plays a causative role in disease progression in each *Mtb*-susceptible mouse model by examining lung bacterial burden in *Ifnar1*-deficient *Sp140*$^{-/-}$, *Nos2*$^{-/-}$, and *Acod1*$^{-/-}$ mice 25 days after *Mtb* infection. As reported previously, global *Ifnar1*-deficiency fully rescued the susceptibility of *Sp140*$^{-/-}$ mice phenocopying the *Mtb* restriction of B6 mice[16,17]; however, *Ifnar1*-deficiency only slightly reduced bacterial burden in *Acod1*$^{-/-}$ mice and did not restore bacterial control in *Nos2*$^{-/-}$ mice (**Fig. 1e, 1f, 1g**). Together, these data suggest that while all three models recapitulate key aspects of human disease, there are major differences in the drivers of susceptibility between these mouse models.

Myeloid cell production of IL-1Ra is a conserved hallmark of Mtb susceptibility

Myeloid cell influx is a hallmark of human and mouse *Mtb* disease[2,3,25,44,45] and neutrophils in particular mediate *Mtb*-susceptibility in *Sp140*$^{-/-}$, *Nos2*$^{-/-}$, and *Acod1*$^{-/-}$ mice[6,17,19]. In line with previous reports, we observed a ~5-fold increase in lung neutrophils and a ~2-4-fold increase in lung monocytes and IMs in *Mtb*-susceptible mice 25 days after *Mtb* infection in each of the three mouse models (**Fig. 2a, Supplementary Fig. 3**). We sought to explore myeloid function in promoting *Mtb* susceptibility by first examining myeloid cell trafficking in *Mtb*-infected lungs from B6 and *Sp140*$^{-/-}$ mice (**Fig. 2b**). Diseased tissue within the lung was defined by the presence of *Mtb* and high cellularity. These features were largely absent from healthy portions of the lung. Diseased areas of the lungs had more macrophages (SIRPα^+ cells) and neutrophils (Ly6G$^+$ cells) than the healthy tissue of the same lungs (**Fig. 2c**). These data indicate that myeloid cells are more abundant in *Mtb*-infected lungs and preferentially traffic to sites of disease within those lungs.

We next sought to define a mechanism by which myeloid cells exacerbate disease upon trafficking to diseased areas of the *Mtb*-infected lungs. We previously demonstrated a role for IL-1Ra in loss of bacterial control in *Mtb*-susceptible *Sst1*^{S} mice[28]. We noted that elevated expression of the *Il1rn* gene (encoding IL-1Ra) was a conserved feature of myeloid cells in *Mtb*-infected B6, *Sp140*$^{-/-}$, *Nos2*$^{-/-}$, and *Acod1*$^{-/-}$ mice. Neutrophils highly expressed *Il1rn* in all the genotypes, while IMs from the susceptible mouse models exhibited elevated *Il1rn* expression relative to B6 (**Fig. 2d**). Analysis of a published scRNA-seq dataset of *Mtb* granulomas from non-human primates[46] mirrored our findings in mice, with neutrophils and macrophages having the highest expression of *IL1RN* in the non-human primate dataset (**Fig. 2e**). Given the conserved nature of IL-1Ra expression, we tested whether *IL1RN* expression could discriminate between active *Mtb* cases and healthy controls in RNA-seq of PBMCs from the TANDEM cohort[43] and observed high sensitivity and specificity for *IL1RN* (**Fig. 2f**). This sensitivity and specificity was slightly improved by including *IL1RN* in a gene signature containing additional known immunosuppressive molecules, such as *IL18BP*[47], *CD274*[48], and *IL10*[49] (**Supplementary Fig. 4**). As IL-1 signaling is regulated by both IL-1Ra and a decoy IL-1R encoded by *Il1r2*, we examined *Il1r2* expression by scRNA-seq and found lower *Il1r2* expression in *Mtb*-infected animals relative to naïve controls, suggesting *Il1r2* does not contribute to *Mtb* outgrowth (**Supplementary Fig. 4**). Given our results, it is likely that the myeloid cell expression of IL-1Ra is conserved across mice, non-human primates, and humans.

IL-1Ra as a conserved mechanism of Mtb susceptibility

Next, we examined whether myeloid cell IL-1Ra expression plays a conserved causative role in susceptibility to *Mtb*. IL-1 is highly expressed in susceptible mouse strains[5], and has been hypothesized to contribute to the susceptibility of *Nos2*$^{-/-}$ mice to *Mtb*[5,6]. However, as we detected high levels of *Il1rn* expression in myeloid cells in *Sp140*$^{-/-}$, *Nos2*$^{-/-}$, and *Acod1*$^{-/-}$ mice, we hypothesized that perhaps the high levels of IL-1 were not functionally protecting the mice due to antagonism by IL-1Ra. Indeed, we previously found that *Mtb*-infected *Sst1*^{S} mice exhibit high levels of IL-1 and yet bacterial burdens in these mice are rescued by enhancement of IL-1 signaling via deletion of *Il1rn*[28]. Likewise, we found that even heterozygous deficiency in *Il1rn* promotes bacterial control in *Sp140*$^{-/-}$ mice (**Fig. 3a**). However, as noted above (**Fig. 1**), *Sp140*$^{-/-}$ and *Sst1*^{S} mice exhibit a strong type I IFN signature that is largely absent from *Nos2*$^{-/-}$ and *Acod1*$^{-/-}$ mice. It was therefore of interest to test whether *Il1rn*-deficiency could also rescue bacterial burdens in *Nos2*$^{-/-}$ and *Acod1*$^{-/-}$ mice. We found that while deletion of one allele of *Il1rn* had no effect on *Mtb* control in *Acod1*$^{-/-}$ mice, complete deletion of *Il1rn* was sufficient for

complete rescue of these mice (**Fig. 3b**). Interestingly, while bacterial burdens were reduced in *Acod1*$^{-/-}$ *Il1rn*$^{-/-}$ mice to levels seen in WT B6 mice, lung neutrophil numbers were still elevated in *Acod1*$^{-/-}$ *Il1rn*$^{-/-}$ mice (**Fig. 3c**). This result implies that the primary detrimental effect of neutrophils during *Mtb* infection may be production of IL-1Ra. In two experiments with a higher and lower dose of *Mtb* inoculum, we also observed partial or complete rescue of bacterial burdens in *Nos2*$^{-/-}$ *Il1rn*$^{-/-}$ mice as compared to *Nos2*$^{-/-}$ mice (**Fig. 3d**). Similar to the *Acod1*$^{-/-}$ mice, no effect of *Ilr1rn* heterozygosity was observed, and the improved bacterial control in *Nos2*$^{-/-}$ *Il1rn*$^{-/-}$ mice did not coincide with a decrease in the number of lung neutrophils (**Fig. 3e**). These results demonstrate a conserved role for IL-1Ra in elevating *Mtb* burdens in three different mouse models.

Both neutrophils and macrophages produce IL-1Ra. Neutrophils are much more abundant in susceptible mice than macrophages, so it might be assumed that neutrophils are the most important source of IL-1Ra. However, prior reports have suggested that the secretion of IL-1Ra by neutrophils is relatively inefficient as compared to macrophages, and specific deletion of IL-1Ra in macrophages is protective during *Candida* infection[50]. Moreover, neutrophil expression of IL-1Ra is constitutive (including in resistant B6 mice) whereas it is induced in IMs. Indeed, IMs in all three susceptible mouse models expressed elevated levels of *Il1rn* relative to wild-type B6 controls (**Fig. 2d**). We therefore hypothesized that macrophage production of IL-1Ra could account for the conserved role of IL-1Ra in inhibiting bacterial control in *Mtb*-susceptible mice. By scRNA-seq, we identified that *Mtb*-infected IMs exhibit the *Spp1*$^{+}$ alternative macrophage activation state that was recently associated with human tumor progression[42] (**Fig. 3f, 3g**). *Il1rn* expression by IMs correlated with the *Spp1*$^{+}$ differentiation state, suggesting that *Spp1*$^{+}$ IMs are a major source of IL-1Ra during *Mtb* infection (**Fig. 3h**). Additionally, *Spp1*$^{+}$ IMs were largely exclusive to the susceptible mouse strains, in line with the elevated *Il1rn* expression of these mice compared to B6 controls (**Fig. 3i**). Based on these expression data, we asked whether *Il1rn* deletion in macrophages would rescue mouse *Mtb* susceptibility. Indeed, macrophage-specific deletion of *Il1rn* in CD64-Cre;*Il1rn*$^{fl/fl}$ mice[51,52] was able to rescue *Sp140*$^{-/-}$ mouse susceptibility (**Fig. 3j**). Together, these data reveal a conserved, myeloid-specific role for IL-1Ra expression in exacerbating *Mtb* disease.

IL-1-enhanced cytokine and chemokine production promotes Mtb control

Given the conserved role for IL-1Ra in exacerbating *Mtb* infection, we were interested in better defining how IL-1 mediates protection against *Mtb*. We first examined IL-1R expression on myeloid cells, as they are the primary reservoir of *Mtb*, and found little to no expression of IL-1R in myeloid cells from naïve and *Mtb*-infected B6, *Sp140*$^{-/-}$, *Nos2*$^{-/-}$, and *Acod1*$^{-/-}$ mice (**Supplementary Fig. 5**). This result is consistent with a previous study showing that IL-1R-deficient macrophages do not exhibit a cell-intrinsic defect in bacterial control in mixed bone marrow (BM) chimera mice[21]. It thus appears that IL-1 mediates its protective effect by signaling in bystander cells that then act non-cell autonomously to promote myeloid cell *Mtb* control. We therefore sought to identify the bystander cells that express IL-1R and the genes regulated by IL-1 in these cells to determine the mechanism by which IL-1 aids in bacterial restriction.

As IL-1 signaling in either hematopoietic or non-hematopoietic cells is sufficient for *Mtb* control early in infection[21,33], we sought to identify potential IL-1 responders in both compartments. Due to the high expression of IL-1Ra in the *Mtb*-susceptible mouse models resulting in IL-1 inhibition, we used B6 mice for examining IL-1 function. Among hematopoietic cells, IL-1 promotes cytokine expression in CD4^{+} T cells[53] and innate lymphoid cells (ILCs)[54,55]. We therefore generated mixed BM chimera mice with a 1:1 mix of WT and *Il1r1*$^{-/-}$ cells that were infected with *Mtb* following immune reconstitution (**Fig. 4a**). In T cells, *Il1r1* was primarily expressed in T helper 17 cells (Th17) with some expression in Type 1 helper cells (Th1; **Fig. 4b, 4c, Supplementary Fig. 6**). Differential scRNA-seq gene expression profiling comparing WT

and *Il1r1*$^{-/-}$ Th17 cells identified *Tnf*, *Gzmb*, and *Ifng* as genes with at least 2-fold greater expression in WT cells that were annotated as potential ligands in the NicheNet database[56] (**Fig. 4d**). Type 3 ILC (ILC3) and IL-17 producing natural killer T (NKT17) cells were the major *Il1r1* expressing innate lymphoid cell populations in *Mtb*-infected lungs, with differential gene expression analysis identifying *Aimp1* and *Cxcl2* as potential ligands in ILC3s; and *Tnf*, *Cxcl10*, *Itgb2*, *Il17a*, *Cxcl2*, and *Rtn4* as potential ligands in NKT17 cells (**Fig. 4e, 4f, 4g, Supplementary Fig. 6**).

Regarding potential non-hematopoietic sensors of IL-1, we first examined sensory neurons as they highly express IL-1R[57], and IL-1 signaling in neurons recruits myeloid cells[58]. As IL-1 signaling in hematopoietic cells is sufficient for early resistance to *Mtb* infection[21,33], we generated BM chimera mice that lacked hematopoietic IL-1R and either had IL-1 receptor in sensory neurons (CD45.1 and Adv$^{+/+}$ *Il1r1*$^{fl/fl}$ recipient mice) or not (Adv$^{cre/+}$ *Il1r1*$^{fl/fl}$ recipient mice). Sensory neuron-specific deletion of *Il1r1* had no effect on bacterial control, suggesting that other non-hematopoietic cells mediate the protective effect of IL-1 against *Mtb* (**Supplementary Fig. 7**). We performed scRNA-seq on BM chimera mice generated by transferring WT BM into lethally irradiated WT and *Il1r1*$^{-/-}$ hosts and then infected the chimeric mice with *Mtb* following immune reconstitution (**Fig. 4h**). Lineage markers used to annotate a scRNA-seq dataset of stromal cells in normal and hyperoxia-damaged murine lungs[59] were used to identify cell populations in our stromal cell scRNA-seq dataset (**Supplementary Fig. 6**). Based on this analysis, *Il1r1* was widely expressed in stromal cells, including in myofibroblasts, fibroblasts, and endothelial cells (**Fig. 4i, 4j**). Differential expression analysis of IL-1-regulated potential ligands, as annotated in NicheNet's database[56], identified *Icam1*, *Il6*, *Ccl2*, and *Wnt11* in myofibroblasts, *Cxcl1*, *Ccl2*, *Il6*, and *Cxcl9* in fibroblasts, and *Icam1* in endothelial cells as IL-1-induced potential ligands (**Fig. 4k**).

The most likely candidates for the protective effect of IL-1 signaling were then identified using NicheNet[56]. For this analysis, we focused on IMs as the receiver cells for the IL-1-regulated ligands as IMs are known to harbor *Mtb* and control the infection[60]. According to the NicheNet ligand-receptor database, the receptors for IFNγ, TNF, IL-6, CCL2, and IL-17 were expressed by IMs (**Supplementary Fig. 8**). While IFNγ and TNF have well-established roles in *Mtb* control[8–10], the contribution of IL-17 has been appreciated more recently[61–64]. Thus, we tested whether IL-1-induced enhancement of IL-17 production was important in IL-1-mediated *Mtb* restriction. This hypothesis was tested by generating mixed BM chimera mice containing BM from *Il17*$^{-/-}$ *Il22*$^{-/-}$ and *Il1r1*$^{-/-}$ mice mixed at a 1:1 ratio as well as control mice (**Fig. 4l**). While the *Il17*$^{-/-}$ *Il22*$^{-/-}$: *Il1r1*$^{-/-}$ BM chimera mice contain cells that can respond to IL-1, as well as cells that can produce IL-17/22, no cell will be able to respond to IL-1 and express IL-17/22. Thus, these chimeras eliminate the ability of IL-1 to amplify IL-17/22 production. The *Il17*$^{-/-}$ *Il22*$^{-/-}$: *Il1r1*$^{-/-}$ BM chimera mice were only slightly more susceptible than control animals, suggesting that an IL-1-mediated increase in IL-17/22 expression is not necessary for IL-1-driven protection (**Fig. 4m**). Therefore, we sought to identify which of the potential ligands were the most likely drivers of IL-1-regulated *Mtb* restriction. We predicted that the signals from bystander cells that help mediate *Mtb* control would result in IM activation. Therefore, we identified genes upregulated in *Spp1*$^{+}$ and activated IMs. NicheNet[56] was then used to calculate the likelihood for each of the potential ligands to induce the transcriptional changes observed in the activated IMs. IFNγ and TNF had the highest scores indicating they are the most likely candidates for how IL-1 protects against *Mtb*, while IL-17 had one of the lowest scores in line with our experimental data (**Supplementary Fig. 8, Fig. 4m**).

Discussion

Mtb infection is a chronic inflammatory disease as evidenced by the induction of a type I/II IFN gene signature up to 12-18 months prior to disease diagnosis[3,65]. While aspects of this inflammatory state—such as the IFNγ response[8,9]—are vital for bacterial control, other components, such as the type I IFN response, exacerbate *Mtb* disease progression[2,17,20]. Our results lead us to hypothesize that the chronic inflammatory nature of *Mtb* infection may hinder bacterial control by promoting immunosuppression. We further propose that this mechanism is conserved across susceptible animal models and in humans. Within the cancer field, a longstanding tenet is that chronic inflammation supports cancer progression[66] with one major mechanism being the recruitment of so-called myeloid-derived suppressor cells (MDSC)[67]. MDSCs are a heterogeneous population in mice and humans, with mouse MDSCs commonly identified based on Gr-1 antibody staining, which binds Ly6C and L6G, markers of monocytes and neutrophils[67]. While monocytes and neutrophils are commonly viewed as proinflammatory cells, MDSCs are immunosuppressive through multiple pathways, including via production of IL-10 and TGFβ[68]. During *Mtb* infection, monocytes and neutrophils are also heavily recruited to the lungs and specifically to sites of bacterial replication (**Fig. 2**). Here we investigated whether myeloid cells play an immunosuppressive role during *Mtb* infection, as has been observed during cancer.

To explore this hypothesis, we first used scRNA-seq to characterize myeloid cells from *Mtb*-infected lungs of three *Mtb*-susceptible mouse lines that all exhibit neutrophil-driven disease, namely, *Sp140*$^{-/-}$, *Nos2*$^{-/-}$, and *Acod1*$^{-/-}$ mice[6,16,17,19]. Gene signatures derived from each of these mice significantly outperform wild-type B6 mice in their ability to discriminate human active *Mtb* cases from healthy controls, suggesting susceptible mice better mimic human disease. Due to the high predictive strength of all three models' gene signatures, it is likely that there are commonalities between the mouse models that are responsible for their discriminatory ability. Initially, we hypothesized that a likely candidate for a shared response to *Mtb* infection was type I IFN, as viral infections and the anti-viral type I IFN response correlate with the severity of *Mtb* disease in humans[2,65,69–71]. A functional role for type I IFNs in driving *Mtb* disease is also observable in mice, as inducers of type I IFNs exacerbate *Mtb* infection in B6 mice[30,72–77] whereas *Ifnar1* deletion rescues bacterial control in *Sst1*^{S} and *Sp140*-deficient mice[16,17,28]. To our surprise, however, type I IFN receptor deletion had little to no effect on bacterial control in *Nos2*$^{-/-}$ and *Acod1*$^{-/-}$ mice (**Fig. 1**), indicating that other pathways drive their *Mtb* susceptibility.

As myeloid cells contribute to disease in each of the tested *Mtb* susceptible mouse models[6,17,19], we sought to define what pathways might be suppressed by myeloid cells to hinder *Mtb* control. IL-1 signaling is a critical pathway for *Mtb* control[21,30–33]. However, the role of IL-1 during *Mtb* pathogenesis has been confusing. Mice deficient in IL-1 signaling are clearly susceptible to *Mtb*[21,30–34], but at the same time, many susceptible mouse models exhibit elevated levels of IL-1[5,28], leading some to propose that IL-1-driven neutrophilic inflammation actually exacerbates *Mtb*[6,26]. Here we propose that the apparently paradoxical effects of IL-1 can be rationalized by an appreciation that high levels of IL-1 cytokine do not necessarily imply high levels of IL-1 signaling. Indeed, the beneficial effects of IL-1 can be neutralized by high levels of the decoy IL-1R or IL-1Ra[78]. Using scRNA-seq, we found that expression of IL-1Ra increased during *Mtb* infection. IL-1Ra was constitutively expressed by neutrophils (**Fig. 2**), as has also been shown for human neutrophils[79], and was preferentially expressed by the alternatively activated *Spp1*$^{+}$ subset of IMs (**Fig. 3**). Interestingly, IMs in all three *Mtb* susceptible mouse lines expressed significantly higher levels of IL-1Ra than B6 mice, which largely lack the *Spp1*$^{+}$ IM population. This expression pattern was conserved across non-human primate *Mtb* granulomas and human PBMCs. We found that myeloid cell expression of IL-1Ra is specifically required for *Mtb* control as macrophage-specific deletion of *Il1rn* was sufficient to rescue the susceptibility of *Sp140*$^{-/-}$ mice. This result correlates with human disease as macrophages are one of the primary IL-1Ra-expressing cell types in human *Mtb* granulomas[80]. Given the high levels of IL-1Ra expression by IMs in the susceptible mouse models, we

predicted that IL-1Ra adversely affects *Mtb* control in each of the susceptible lines, which was confirmed by rescuing bacterial control in all three mouse lines with global deletion of IL-1Ra. This result was highly unexpected given prior claims that excessive IL-1 signaling is detrimental during *Mtb* infection[4] particularly following the onset of the adaptive immune response in *Nos2*$^{-/-}$ mice[5,6]. Our results instead suggest that the lack of bacterial control in highly inflamed *Mtb*-susceptible mouse models, such as *Acod1*$^{-/-}$ and *Nos2*$^{-/-}$ mice, is actually due to insufficient rather than excessive IL-1 signaling. Our result is in line with the susceptibility of mice deficient in IL-1 signaling[21,30,32,33], as well as with anecdotal evidence in humans reporting *Mtb* reactivation following IL-1Ra (Anakinra) treatment[81].

The mechanism by which IL-1 exerts its protective effects remains the subject of intensive study. In line with the limited myeloid cell *Il1r1* expression in our scRNA-seq dataset, IL-1 has been proposed to act on uninfected bystander cells that then promote myeloid cell *Mtb* control[21,33]. IL-1 signaling in either hematopoietic or non-hematopoietic bystander cells is sufficient to mediate protection during early infection[21,33]. Yet the mechanism for IL-1-mediated protection is not fully established, with eicosanoid regulation and synergistic interactions between IL-1 and TNF being two potential mechanisms[30,33]. Our BM chimera scRNA-seq experiments identified multiple IL-1-induced cytokines and chemokines as potential activators of *Mtb*-harboring IMs, with the most likely being *Ifng* and *Tnf*, two cytokines known to play a key role in *Mtb* restriction[8–10]. As IL-1 signaling in CD4^{+} T cells directly promotes cytokine production[53], it is likely that IL-1 directly enhances *Ifng* and *Tnf* production by T cells and ILCs throughout *Mtb* infection. During *Legionella pneumophila* infection, IL-1 acts on type II alveolar epithelial cells inducing their expression of GM-CSF[82], another cytokine that activates macrophages with an established contribution to *Mtb* control[83–85]. Our stromal scRNA-seq dataset had limited coverage of epithelial cells so we were unable to observe whether IL-1 also induces GM-CSF expression in type II alveolar cells during *Mtb* infection. However, it is likely that this mechanism is conserved between *Legionella* and *Mtb* infections given the critical role played by GM-CSF and stromal cell IL-1 signaling in both infections.

In summary, our data support a model in which initial loss of bacterial control, whether due to a type I IFN response, *Nos2*-, or *Acod1*-deficiency, results in myeloid cell influx into *Mtb*-infected lungs. The incoming monocytes differentiate into IMs that adopt the *Spp1*$^{+}$ activation state in animals with chronic inflammation, which correlates with the upregulation of IL-1Ra. This high level of IL-1Ra expression hinders critical IL-1 signaling in hematopoietic and non-hematopoietic cells, reducing the production of *Mtb*-restrictive cytokines, such as TNF and IFNγ. The blockade of IL-1 thus generates a positive feedback loop where *Mtb*-harboring myeloid cells are unable to restrict the bacteria. Enhanced bacterial replication leads to the influx of yet more myeloid cells and further increases IL-1Ra levels. Our results are largely consistent with a recently proposed 'tipping-point' model of tuberculosis[86], which proposes that neutrophils cause a feedforward loop exacerbating disease even if they are not the initial driver of loss of *Mtb* restriction. In this study, we recapitulate this model and additionally elucidate key molecular and cellular players that orchestrate the tipping point.

It remains unclear whether IL-1 signaling could be manipulated therapeutically during human TB. Although we find that enhancement of IL-1 signaling increases bacterial control, excessive IL-1 signaling can also cause significant pathology. Indeed, although myeloid cell production of IL-1Ra impairs bacterial control, IL-1Ra expression likely evolved to limit host pathology and therefore may be beneficial in many cases. Additionally, IL-1Ra is likely just one of many molecules that dictate the balance between bacterial control and host pathology during *Mtb* infection. For example, our gene signatures for the *Mtb*-susceptible mouse lines (but not the *Mtb*-restrictive B6 mice) contain other known immunosuppressive molecules, such as *Cd274* and *Il18bp*. Overall, our results therefore suggest that host-directed therapy to *Mtb* may require a delicate balance between anti-bacterial and host-tolerance mechanisms.

Acknowledgments

We thank members of the Vance, Barton, Stanley, and Cox laboratories for advice and discussions; the Stanley and Cox labs for the shared operation of the UC Berkeley BSL-3 and ABSL-3 labs; S. Gupta and P. Khatri for advice on analysis of human cohorts; B. Malissen, S. Khader, and Y. Belkaid for mice; P. Dietzen, R. Chavez, J. Morales, and J. Rodriguez for technical assistance; A. Valeros, H. Nolla, and K. Heydari of the UC Berkeley Cancer Research Laboratory Flow Cytometry facility for assistance with flow cytometry; H. Aaron and F. Ives of the UC Berkeley Cancer Research Laboratory Molecular Imaging Center (RRID:SCR_017852) for assistance with confocal microscopy (supported by the Helen Wills Neuroscience Institute). Model figures were created with BioRender.com. D.I.K. was supported by an NIH Postdoctoral Fellowship (F32HL158250). R.E.V. is an Investigator of the Howard Hughes Medical Institute and is supported by NIH grants AI075039, AI063302 and AI155634.

Author Contributions

Conceptualization: D.I.K. and R.E.V. Investigation: D.I.K., O.V.L., and D.X.J. Data analysis: D.I.K. and O.V.L. Methodology: S.S. Resources: C.G. and D.L.J. Writing: D.I.K. and R.E.V. with input from all co-authors. Funding acquisition: R.E.V. Supervision: R.E.V.

Declaration of Interests

R.E.V. consults for Tempest Therapeutics and X-biotix Therapeutics.

Figure Legends

Figure 1. *Nos2*- and *Acod1*-deficient mice mimic human *Mtb* progression but do not exhibit type I interferon-driven susceptibility. (**a**) Visualizing lung myeloid cell populations in a scRNA-seq dataset of cells from *Mtb*-infected B6, *Nos2*$^{-/-}$, *Acod1*$^{-/-}$, and *Sp140*$^{-/-}$ mice (n = 3 per genotype). (**b**) ROC curves of the ability of genes induced by *Mtb* infection in B6, *Nos2*$^{-/-}$, *Acod1*$^{-/-}$, or *Sp140*$^{-/-}$ mice to stratify human active *Mtb* patients (n = 151) and healthy controls (n = 98) in the TANDEM cohort (analysis of GSE114192). (**c**) UMAP plot and (**d**) quantification of myeloid cells undergoing type I interferon and/or IFNγ signaling in the lungs of naïve or *Mtb*-infected B6, *Nos2*$^{-/-}$, *Acod1*$^{-/-}$, or *Sp140*$^{-/-}$ mice (n = 3 per genotype and infection status). (**e**) Lung bacterial burden in B6 (n = 10), *Sp140*$^{-/-}$ (n = 11), and *Sp140*$^{-/-}$ *Ifnar1*$^{-/-}$ (n = 12) mice infected with *Mtb*. (**f**) Lung bacterial burden in littermate control (n = 16), *Acod1*$^{-/-}$ *Ifnar1*$^{+/-}$ (n = 12), and *Acod1*$^{-/-}$ *Ifnar1*$^{-/-}$ (n = 9) mice infected with *Mtb*. (**g**) Lung bacterial burden in *Nos2*$^{+/+}$ littermate control (n = 4), *Nos2*$^{+/-}$ littermate control (n = 9), *Nos2*$^{+/-}$ *Ifnar1*$^{-/-}$ (n = 10), *Nos2*$^{-/-}$ (n = 8), and *Nos2*$^{-/-}$ *Ifnar1*$^{-/-}$ (n = 11) mice infected with *Mtb*. Lungs were analyzed 25-27 days after *Mtb*-Wasabi infection. The bars in (e), (f), and (g) represent the median. Pooled data from two independent experiments are shown in (e), (f), and (g). Statistical significance in (d), (e), (f), and (g) by one-way ANOVA with Tukey's multiple comparison test. *$p < 0.05$, **$p < 0.01$, ***$p < 0.001$, ****$p < 0.0001$.

Figure 2. Neutrophils and interstitial macrophages localize to diseased tissue and are abundant, major expressors of IL-1Ra. (**a**) Number of neutrophils, monocytes, IMs, and AMs in the lungs of *Mtb*-infected *Sp140*$^{-/-}$ (n = 13), *Sp140*$^{-/-}$ *Ifnar1*$^{-/-}$ (n = 11), *Acod1*$^{+/+}$ (n = 7), *Acod1*$^{+/-}$ (n = 6), *Acod1*$^{-/-}$ (n = 12), *Nos2*$^{+/+}$ (n = 4), *Nos2*$^{+/-}$ (n = 7), and *Nos2*$^{-/-}$ (n = 8) mice. (**b**) Representative images and (**c**) image quantification of *Mtb* (*Mtb*-mCherry^{+}, pink), macrophages (SIRPα^{+}, blue), and neutrophils (Ly6G^{+}, red) in diseased and healthy portions of *Mtb*-infected

B6 (n = 5) and *Sp140*$^{-/-}$ lungs (n = 6). (**d**) *Il1rn* expression measured by scRNA-seq of *Mtb*-infected myeloid cell populations in the lungs of B6, *Nos2*$^{-/-}$, *Acod1*$^{-/-}$, and *Sp140*$^{-/-}$ mice (n = 3 per genotype). (**e**) IL1RN expression as measured by scRNA-seq of *Mtb* granulomas from non-human primates 10 weeks post-infection (Analysis of GSE200151). (**f**) ROC curve depicting the ability of *IL1RN* expression to stratify human active *Mtb* patients (n = 151) and healthy controls (n = 98) in the TANDEM cohort (analysis of GSE114192). Lungs were analyzed for the experiments depicted in (a) – (d) 24-26 days after *Mtb*-Wasabi or *Mtb*-mCherry infection. The bars in (a) represent the median. Pooled data from two independent experiments are shown in (a) and (c). Statistical significance in (d) was calculated with the Wilcoxon Rank-Sum test with Bonferroni correction, in (a) by one-way ANOVA with Tukey's multiple comparison test, and in (c) by paired t test. *p < 0.05, **p < 0.01, ***p < 0.001, ****p < 0.0001.

Figure 3. Macrophage-derived IL-1Ra is a conserved driver of *Mtb* susceptibility. (**a**) Lung bacterial burden in *Sp140*$^{-/-}$ (n = 14), *Sp140*$^{-/-}$ *Il1rn* $^{+/-}$ (n = 16), *Sp140*$^{-/-}$ *Il1rn*$^{-/-}$ (n = 8), and *Sp140*$^{-/-}$ *Ifnar1*$^{-/-}$ mice (n = 15) following *Mtb* infection. (**b**) Lung bacterial burden and (**c**) neutrophil numbers in *Acod1*$^{+/-}$ *Il1rn*$^{+/+}$ (n = 7), *Acod1*$^{-/-}$ *Il1rn*$^{+/+}$ (n = 14), *Acod1*$^{-/-}$ *Il1rn*$^{+/-}$ (n = 28), and *Acod1*$^{-/-}$ *Il1rn*$^{-/-}$ (n = 8) mice following *Mtb* infection. (**d**) Lung bacterial burden and (**e**) neutrophil numbers in Nos2-sufficient controls (n = 11), *Nos2*$^{-/-}$ *Il1rn*$^{+/+}$ (n = 8-16), *Nos2*$^{-/-}$ *Il1rn*$^{+/-}$ (n = 8-18), *Nos2*$^{-/-}$ *Il1rn*$^{-/-}$ (n = 6-19), littermate control (n = 6) and B6 (n = 5) mice following *Mtb* infection. (**f**) Lung *Mtb*-infected monocyte and macrophage expression of *Spp1* and *Cxcl9*, (**g**) the resulting cell annotation, and (**h**) *Il1rn* expression for cells from B6, *Nos2*$^{-/-}$, *Acod1*$^{-/-}$, and *Sp140*$^{-/-}$ mice combined (n = 3 per genotype. (**i**) Lung *Mtb*-infected monocyte and macrophage populations visualized separately for B6, *Nos2*$^{-/-}$, *Acod1*$^{-/-}$, and *Sp140*$^{-/-}$ mice (n = 3 per genotype). (**j**) Lung *Mtb* burden in *Sp140*$^{+/-}$ littermate control (n = 13), *Sp140*$^{-/-}$ littermate control (n = 11), and *Sp140*$^{-/-}$ *Il1rn*$^{fl/fl}$ *CD64*$^{cre+}$ (n = 13) mice. Lungs were analyzed 24-26 days after *Mtb*-Wasabi infection. The bars in (a) – (e) and (j) represent the median. Pooled data from two independent experiments are shown in (a) – (e) and (j). Statistical significance in (a) - (e) and (j) was calculated by one-way ANOVA with Tukey's multiple comparison test. *p < 0.05, **p < 0.01, ***p < 0.001, ****p < 0.0001.

Figure 4. IL-1 enhances cytokine and chemokine expression by Th17, NKT17, and ILC3 as well as stromal cells. (**a**) Schematic of the BM chimera mice used in panels (b) – (g). (**b**) T cell populations and (**c**) their expression of *Il1r1* in the *Mtb*-infected lungs of the BM chimera mice. (**d**) Volcano plot of the differentially expressed genes in the WT Th17 cells relative to *Il1r1*$^{-/-}$ Th17 cells during *Mtb* infection. (**e**) Innate lymphoid cell populations and (**f**) their expression of *Il1r1* in the *Mtb*-infected lungs of the BM chimera mice. (**g**) Differentially expressed genes in the WT ILC3 and NKT17 cells relative to *Il1r1*$^{-/-}$ cells during *Mtb* infection. (**h**) Schematic of the BM chimera mice used in panels (i) – (k). (**i**) Non-hematopoietic cell populations and (**j**) their expression of *Il1r1* in the *Mtb*-infected lungs of the BM chimera mice. (**k**) Differentially expressed genes in the WT myofibroblast, fibroblast, and endothelial cells relative to *Il1r1*$^{-/-}$ cells during *Mtb* infection. (**l**) Schematic of the BM chimera mice used in panel (m). (**m**) Lung *Mtb* burden in BM chimera mice that received *Il1r1*$^{-/-}$: CD45.1 mixed BM (n = 8), *Il1r1*$^{-/-}$: *Il17*$^{-/-}$ *Il22*$^{-/-}$ mixed BM (n = 10), or *Il1r1*$^{-/-}$ BM (n = 13). Lungs were analyzed 25 days after *Mtb*-Wasabi infection. The bars in (m) represent the median. Pooled data from two independent experiments are shown in (m). Statistical significance in (d), (g), and (k) was calculated with the Wilcoxon Rank-Sum test with Bonferroni correction and in (m) by one-way ANOVA with Tukey's multiple comparison test. *p < 0.05.

Materials and Methods

Mice

Following University of California Berkeley Institutional Animal Care and Use Committee regulatory standards, mice were housed at 23°C with a 12-hour light-dark cycle and maintained under specific pathogen-free conditions. Male and female mice were used for experiments. Mice were age-matched with littermate controls used when possible and 6-12 weeks old at the start of the infections. C57BL/6 (B6), B6.129S2-Ifnar1^{tm1Agt}/Mmjax (*Ifnar1*$^{-/-}$)[87], B6.SJL-*Ptprc*^{a} *Pepc*^{b}/BoyJ (CD45.1)[88], B6.129S7-*Il1r1*^{tm1Imx}/J (*Il1r1*$^{-/-}$)[89], B6.129(Cg)-*Il1r1*$^{tm1.1Rbl}$/J (*Il1r1*$^{fl/fl}$)[90], B6.129P2-*Avil*$^{tm2(cre)Fawa}$/J (Adv^{Cre})[91], B6.129P2-*Nos2*^{tm1Lau}/J (*Nos2*$^{-/-}$)[92], and C57BL/6NJ-*Acod1*$^{em1(IMPC)J}$/J (*Acod1*$^{-/-}$) mice were purchased from Jackson Laboratories. B6-Fcgr1^{tm2Ciphe} (CD64^{Cre})[51] mice were a gift from B. Malissen at Centre d'Immunologie de Marseille Luminy and were provided by Y. Belkaid at the National Institutes of Health. BM from *Il17*$^{-/-}$ *Il22*$^{-/-}$ mice was a gift from S. Khader at the University of Chicago. Il1rn$^{tm1.1Cga}$ (*Il1rn*^{fl})[52] were generated by Cem Gabay at the University of Geneva and were provided by A. Luster at Massachusetts General Hospital. *Sp140*$^{-/-}$ mice were previously generated in-house[16]. *Sp140*$^{-/-}$ *Ifnar1*$^{-/-}$, *Acod1*$^{-/-}$ *Ifnar1*$^{-/-}$, and *Nos2*$^{-/-}$ *Ifnar1*$^{-/-}$ mice were generated by crossing *Sp140*$^{-/-}$, *Acod1*$^{-/-}$, and *Nos2*$^{-/-}$ mice with *Ifnar1*$^{-/-}$ mice in-house, respectively. *Sp140*$^{-/-}$, *Acod1*$^{-/-}$, and *Nos2*$^{-/-}$ mice were crossed in-house with *Il1rn*$^{-/-}$ mice to generate *Sp140*$^{-/-}$ *Il1rn*$^{-/-}$, *Acod1*$^{-/-}$ *Il1rn*$^{-/-}$, and *Nos2*$^{-/-}$ *Il1rn*$^{-/-}$ mice. *Sp140*$^{-/-}$ *Il1rn*^{fl} CD64^{Cre} mice were generated by crossing *Sp140*$^{-/-}$ mice with *Il1rn*^{fl} and CD64^{Cre} mice in-house. Adv^{Cre} *Il1r1*$^{fl/fl}$ and CD64^{Cre} *Il1r1*$^{fl/fl}$ mice were generated by crossing Adv^{Cre} and CD64^{Cre} mice with *Il1r1*$^{fl/fl}$ mice in-house.

Bone marrow chimera mice

Adult mice were lethally irradiated with a Precision X-Rad320 X-Ray irradiator (North Branford, CT) using a split dose of 500 rads each round with irradiation occurring 4-12 hours apart. BM from donor mice indicated in the figures was prepared by mashing femurs with a mortar and pestle to generate a single cell suspension. Red blood cells were then lysed with Ack lysis buffer (Thermo Fisher Scientific). The cells were then diluted in PBS and 1×10^7 cells (either all one genotype or a 1 : 1 mix of two genotypes for mixed BM chimera mice) were retro-orbitally injected into each recipient mouse. Mice were housed for at least 8 weeks post-injection to reconstitute prior to their use in experiments.

Mtb infections

Mtb expressing Wasabi (*Mtb*-Wasabi) and *Mtb*-mCherry were generated using *Mtb* Erdman, a gift from S. A. Stanley, that had been passaged 2 or fewer times *in vitro*. *Mtb* was transformed with the pTEC15 plasmid (a gift from Lalita Ramakrishnan; Addgene plasmid # 30174)[93] or the pMSP12::mCherry plasmid (a gift from Lalita Ramakrishnan; Addgene plasmid # 30167) to generate *Mtb*-Wasabi and *Mtb*-mCherry, respectively. For the transformation, *Mtb* was cultured in Middlebrook 7H9 liquid medium supplemented with 10% albumin-dextrose-saline, 0.4% glycerol, and 0.05% Tween-80 for 5 days at 37°C then washed in 10% glycerol to remove salts. Washed *Mtb* was electroporated with 1 µg DNA using a 2 mm electroporation cuvette and the following settings: 2500 volts, 1000 Ohms, 25 µF. Electroporated Mtb was grown on 7H11 plates supplemented with 10% oleic acid, albumin, dextrose, and catalase, 0.5% glycerol, and either 200 µg / mL Hygromycin for *Mtb*-Wasabi or 50 µg / mL Kanamycin for *Mtb*-mCherry for 3-4 weeks at 37°C. Colonies were picked and cultured in 10 mL inkwell flasks for 7 days at 37°C and then expanded into a 100 mL culture for 4-5 days at 37°C using 7H9 medium supplemented with 10% albumin-dextrose-saline, 0.4% glycerol, 0.05% Tween-80, and either Hygromycin for *Mtb*-Wasabi or Kanamycin for *Mtb*-mCherry. At log phase, the Mtb was filtered through a 5 µm syringe filter and frozen in 1 mL aliquots in 10% glycerol. Frozen cultures were diluted in distilled

H_20 to an O.D. of 0.0017 and then aerosolized with an inhalation exposure system (Glas-Col, Terre Haute, IN) thereby delivering ~10-100 Mtb per mouse as determined by plating lungs day 1 post-infection to assess bacterial burden.

Tissue Processing for CFU and Flow cytometry

Mice were harvested at 24-27 days following Mtb infection. Lungs were collected in gentleMACS C tube (Miltenyi Biotec) containing 3 mL of RPMI media with 70 µg / mL of Liberase TM (Roche) and 30 µg / mL of DNase I (Roche) and then processed using the lung_01 setting on a gentleMACS (Miltenyi Biotec). Samples were then digested at 37°C for 30 minutes before being homogenized with the lung_02 setting on the gentleMACS. 2 mL of PBS with 20% Newborn Calf Serum (Thermo Fisher Scientific) were added to each sample to quench the digest before samples were filtered through 70 µm SmartStrainers (Miltenyi Biotec).

Measuring Bacterial Burden

Mtb burden was assessed by serial dilution of the lung single cell suspension in phosphate-buffered saline (PBS) with 0.05% Tween-80. The dilutions were plated on 7H11 plates supplemented with 10% oleic acid, albumin, dextrose, and catalase and 0.5% glycerol and colonies were counted 3 weeks after plating.

Flow Cytometry

Flow cytometry was performed by staining 100 uLs of lung single cell suspension with antibodies in PBS with 2% Newborn Calf Serum and 0.05% Sodium azide. A fixable viability dye (Ghost Dye Violet 510 or 540 or Red 780; Tonbo Biosciences), Super Bright Complete Staining Buffer (Thermo Fisher Scientific), and True-Stain Monocyte Blocker (BioLegend) were also added to every sample during surface antibody staining. Surface stains were incubated for 30 minutes to an hour at room temperature using a selection of the following antibodies: TruStain FcX PLUS (S17011E, BioLegend), BUV496-labeled CD45 (30-F11, BD Biosciences), BUV395-labeled CD11b (M1/70, BD Biosciences), BUV737-labeled CD11c (HL3, BD Biosciences), APC-R700-labeled Siglec F (E50-2440, BD Biosciences), PE-labeled MerTK (DS5MMER, Thermo Fisher Scientific), Super Bright 645-labeled MHC II (M5/114.15.2, Thermo Fisher Scientific), BV421-labeled PD-L1 (MIH5, BD Biosciences), BV711-labeled Ly6C (HK1.4 , BioLegend), PE-Cy7-labeled MerTK (DS5MMER, Thermo Fisher Scientific), APC-labeled CD64 (X54-5/7.1, BioLegend), BUV563-labeled Ly6G (1A8, BD Biosciences), BV605-labeled MHC II (M5/114.15.2, BioLegend), Percp-Cy5.5-labeled CD9 (MZ3, BioLegend), eFluor 450-labeled Ly6D (49-H4, Thermo Fisher Scientific), BV480-labeled Fcer1a (MAR-1, BD Biosciences), BV650-labeled CD8 (53-6.7, BioLegend), BV785-labeled CD16.2 (9E9, BioLegend), AF594-labeled TREM2 (237920, R&D systems), AF647-labeled XCR1 (ZET, XCR1), APC-Fire 750-labeled CD19 (6D5, BioLegend), APC-Fire 750-labeled CD90.2 (30-H12, BioLegend), BUV615-labeled SIRP (P84, BD Biosciences), BUV661-labeled B220 (RA3-6B2, BD Biosciences), BUV805-labeled CD26 (H194-112, BD Biosciences). Following surface staining, samples were washed with PBS with 2% Newborn Calf Serum and 0.05% Sodium azide and then fixed for 20 minutes at room temperature with cytofix/cytoperm (BD biosciences) prior to removal from the BSL3. If intracellular staining was performed, samples were incubated overnight at 4°C with combinations of the following antibodies: PE-Cy7-labeled CD63 (NVG-2, BioLegend), AF532-labeled iNOS (CXNFT, Thermo Fisher Scientific), and Percp-eFluor 710-labeled iNOS (CXNFT, Thermo Fisher Scientific). After washing out the intracellular stain, each sample received AccuCheck Counting Beads (Invitrogen) and was then analyzed on an Aurora (Cytek) flow cytometer. Data were analyzed with Flowjo version 10 (BD Biosciences).

Confocal microscopy

A Zeiss LSM 880 laser scanning confocal microscope with 405, 458, 488, 514, 561, 594, and 633 lasers, with two photomultiplier detectors, a 34-channel GaASP spectral detector system, and a 2-channel AiryScan detector was used for microscopy. 20 µm sections were prepared from paraformaldehyde-fixed lungs from *Mtb*-mCherry-infected B6 and *Sp140*$^{-/-}$ mice. The sections were stained overnight at 4°C with the following antibodies: BV421-labeled SIRP (P84, BD Biosciences), Pacific Blue–labeled B220 (RA3-6B2, BioLegend), eF506-labeled CD4 (RM4-5, BioLegend), and AF647-labeled Ly6G (1A8, BioLegend). Diseased and healthy lesions were identified in stained sections with a 5× air objective and then imaged as a 20 µm z-stack acquired at a 1.5 µm step size with a 63× oil immersion objective lens with a numerical aperture of 1.4. The 63× oil immersion objective lens with a numerical aperture of 1.4 was also used to image single color-stained Ultracomp eBeads Plus (Thermo Fisher Scientific) for generating a compensation matrix.

Image processing and histo-cytometry analysis

The Generate Compensations Matrix script[94] was used in ImageJ to create a compensation matrix based on the single color-stained control images of the Ultracomp eBeads Plus (Thermo Fisher Scientific). The resulting compensation matrix was used for spectral unmixing of the lung images using Chrysalis software[94], which was also used to rescale the data and generate new channels based on mathematical operations performed on existing channels. Imaris 9.9.1 (Bitplane) was used on the processed lung images to digitally identify cells based on protein expression using the surface creation tool[95]. Statistics for the identified cells were exported from Imaris and then imported into FlowJo version 10 (BD Biosciences) for quantitative image analysis.

Sorting Immune Cells for scRNA-seq analysis

For the myeloid dataset, Lungs from 3 *Mtb*-Wasabi-infected as well as 3 naïve *Acod1*$^{-/-}$ and *Nos2*$^{-/-}$ mice were processed as described for CFU and flow cytometry analysis 25 days after infection with the following slight modification: 3 minutes before harvesting, 0.25 µg of TotalSeq-A-labeled CD45.2 (104, BioLegend) was intravenously injected into each mouse to label cells in the vasculature[96]. Surface staining of lung single cell suspensions was performed in PBS with 2% Newborn Calf Serum on ice for 30 minutes with the following antibodies: TruStain FcX PLUS (S17011E, BioLegend), APC-labeled Ly6G (1A8, BioLegend), APC-labeled CD64 (X54-5/7.1, BioLegend), and TotalSeq-A-labeled Ly6G (1A8, BioLegend). Magnetic enrichment was then performed with the EasySep APC Positive Selection Kit II (StemCell Technologies) and MojoSort Magnets (BioLegend) to increase the frequency of myeloid cells within the sample prior to sorting. Following enrichment, samples were stained on ice for 45 minutes in PBS with 2% Newborn Calf Serum and True-Stain Monocyte Blocker (BioLegend) using a combination of the following antibodies: TotalSeq-A-labeled Ly6C (HK1.4, BioLegend), TotalSeq-A-labeled CD44 (IM7, BioLegend), TotalSeq-A-labeled CD274 (MIH6 , BioLegend), TotalSeq-A-labeled Siglec F (S17007L, BioLegend), TotalSeq-A-labeled CSF1R (AFS98, BioLegend), TotalSeq-A-labeled CD11b (M1/70, BioLegend), TotalSeq-A-labeled CD86 (GL-1, BioLegend), TotalSeq-A-labeled MHC II (M5/114.15.2, BioLegend), TotalSeq-A-labeled CX3CR1 (SA011F11, BioLegend), TotalSeq-A-labeled CD11c (N418, BioLegend), TotalSeq-A-labeled CCR2 (SA203G11, BioLegend), TotalSeq-A-labeled CD62L (MEL-14, BioLegend), anti-mouse TotalSeq-A Hashtag antibody (1-6; BioLegend), PE-labeled Siglec F (S17007L, BioLegend), Pacific Blue-labeled B220 (RA3-6B2, BioLegend), and Pacific Blue-labeled CD90.2 (53-2.1,

BioLegend). The TotalSeq-A-labeled antibodies detect protein expression in the scRNA-seq dataset, while the Hashtag antibodies allow several samples to be multiplexed together in a single lane on a 10X Genomics Chromium Next GEM Chip[97]. After staining, the samples were incubated with Sytox Blue Dead Cell Stain (Thermo Fisher Scientific) and sort purified using a 100 µm sorting chip in a 4 laser SH-800 cell sorter (Sony) on the purity setting. For *Mtb*-infected mice, *Mtb*-infected cells and bystander myeloid cells were individually purified, while samples from naïve lungs were sorted as macrophages and a mixture of neutrophils and monocytes that were then combined at a 1:2 ratio for greater representation of macrophages in the scRNA-seq dataset.

The stromal cell dataset was generated by infecting BM chimera mice made by transferring CD45.1 BM into lethally irradiated B6 or *Il1r1*$^{-/-}$ hosts with *Mtb* 8 weeks post-reconstitution. Lungs from the infected animals as well as naïve chimera mice were harvested and processed as described for CFU and flow cytometry analysis. Ack lysing buffer (Thermo Fisher Scientific) was used to lyse the red blood cells in the samples, which were then stained for 30 minutes on ice with TruStain FcX PLUS (S17011E, BioLegend) and PE-Cy7-labeled CD45 (30-F11, BioLegend) antibody. The EasySep PE Positive Selection Kit II (StemCell Technologies) and MojoSort Magnets (BioLegend) were used to perform negative selection to enrich the CD45^{-} non-hematopoietic cells. The enriched cells were incubated with Sytox Green Dead Cell Stain (Thermo Fisher Scientific) and live CD45^{-} were sort purified using a 130 µm sorting chip in a 4 laser SH-800 cell sorter (Sony) on the purity setting.

The T cell and ILC datasets were generated by *Mtb* infection of mixed BM chimera mice generated by transferring WT CD45.1/2 and *Il1r1*$^{-/-}$ BM into lethally irradiated CD45.1 mice. Lungs were harvested 25 days post-infection and processed as described for measuring CFU and performing flow cytometry. Three mice were used for the T cell dataset, while the rarity of the ILCs required pooling lungs into 3 samples (2 samples containing 5 lungs and 1 sample containing 6 lungs). The T cell samples were treated with Ack lysing buffer (Thermo Fisher Scientific) to lyse the red blood cells and then stained on ice for 30 minutes with the following antibodies: BV421-labeled CD45.1 (A20, BioLegend), BV785-labeled CD45.2 (104, BioLegend), PE-labeled CD3e (17A2, BioLegend), APC-labeled CD11b (M1/70, Cytek), APC-labeled CD11c (N418, Cytek), APC-labeled CD19 (1D3, Cytek), TotalSeq-A-labeled Ly6C (HK1.4, BioLegend), TotalSeq-A-labeled CD44 (IM7, BioLegend), TotalSeq-A-labeled CD274 (MIH6 , BioLegend), TotalSeq-A-labeled CX3CR1 (SA011F11, BioLegend), TotalSeq-A-labeled CD62L (MEL-14, BioLegend), TotalSeq-A-labeled TCRβ (H57-597, BioLegend), TotalSeq-A-labeled CD49a (, BioLegend), TotalSeq-A-labeled CD49a (HMα1, BioLegend), TotalSeq-A-labeled NKp46 (29A1.4, BioLegend), TotalSeq-A-labeled CD4 (RM4-5, BioLegend), TotalSeq-A-labeled ST2 (DIH9, BioLegend), TotalSeq-A-labeled CD25 (PC61, BioLegend), TotalSeq-A-labeled CD45.1 (A20, BioLegend), TotalSeq-A-labeled CD45.2 (104, BioLegend), TotalSeq-A-labeled CD8a (53-6.7, BioLegend), TotalSeq-A-labeled CXCR5 (L138D7, BioLegend), TotalSeq-A-labeled CCR6 (29-2L17, BioLegend), and anti-mouse TotalSeq-A Hashtag antibody (1-3; BioLegend). The stained T cell samples were then incubated with Sytox Green Dead Cell Stain (Thermo Fisher Scientific) and T cells (Live CD3e^{+} CD11b^{-} CD11c^{-} CD19^{-} CD45.1^{+} or CD45.2^{+} cells) were sort purified using a 100 µm sorting chip in a 4 laser SH-800 cell sorter (Sony) on the purity setting.

The ILC samples treated with Ack lysing buffer (Thermo Fisher Scientific) were stained on ice for 25 minutes with the following panel of lineage-specific antibodies: Biotin-labeled TER-119 (TER-119, BioLegend), Biotin-labeled GR-1 (RB6-8C5, BioLegend), Biotin-labeled CD3e (145-2C11, BioLegend), Biotin-labeled CD11b (M1/70, BioLegend), Biotin-labeled B220 (RA3-6B2, BioLegend), and Biotin-labeled TCRγ/δ (GL3, BioLegend). Lineage^{-} cells were enriched by negative selection using the EasySep Streptavidin RapidSpheres Isolation Kit (StemCell Technologies) and MojoSort Magnets (BioLegend). Enriched samples were then stained on ice for 30 minutes with the following antibodies: BV421-labeled CD45.1 (A20, BioLegend), BV785-labeled CD45.2 (104, BioLegend), PE-labeled CD127 (A7R34, BioLegend), Alexa Fluor 700-

labeled CD127 (30-H12, BioLegend), Biotin-labeled CD5 (53-7.3, BioLegend), Biotin-labeled TCRβ (H57-597, BioLegend), TotalSeq-A-labeled Ly6C (HK1.4, BioLegend), TotalSeq-A-labeled CD44 (IM7, BioLegend), TotalSeq-A-labeled CD274 (MIH6 , BioLegend), TotalSeq-A-labeled CX3CR1 (SA011F11, BioLegend), TotalSeq-A-labeled CD62L (MEL-14, BioLegend), TotalSeq-A-labeled TCRβ (H57-597, BioLegend), TotalSeq-A-labeled CD49a (, BioLegend), TotalSeq-A-labeled CD49a (HMα1, BioLegend), TotalSeq-A-labeled NKp46 (29A1.4, BioLegend), TotalSeq-A-labeled CD4 (RM4-5, BioLegend), TotalSeq-A-labeled ST2 (DIH9, BioLegend), TotalSeq-A-labeled CD25 (PC61, BioLegend), TotalSeq-A-labeled CD45.1 (A20, BioLegend), TotalSeq-A-labeled CD45.2 (104, BioLegend), TotalSeq-A-labeled CD8a (53-6.7, BioLegend), TotalSeq-A-labeled CXCR5 (L138D7, BioLegend), TotalSeq-A-labeled CCR6 (29-2L17, BioLegend), and anti-mouse TotalSeq-A Hashtag antibody (4-6; BioLegend). The enriched samples were then stained with APC-labeled Streptavidin (BioLegend) for 15 minutes on ice before being stained with Sytox Green Dead Cell Stain (Thermo Fisher Scientific). ILCs (Lineage^{-} IL-7Ra^{+} CD90.2^{+} CD45.1^{+} or CD45.2^{+} cells) were sort purified using a 100 µm sorting chip in a 4 laser SH-800 cell sorter (Sony) on the purity setting.

Single cell RNA: Library generation and sequencing.

The v3.1 chemistry Chromium Single Cell 3' Reagent Kit (10X Genomics) was used to generate scRNA-seq libraries using the CITE-seq protocol[39] modifications for the myeloid, T, and innate lymphoid cell libraries and the standard 10X protocol for the stromal cell library. The myeloid cell dataset required three lanes of a Chromium Next GEM Chip were used, with lane 1 containing naïve cells, lane 2 containing *Mtb*-infected cells, and lane 3 containing the bystander cells from the 3 *Acod1*$^{-/-}$ and 3 *Nos2*$^{-/-}$ mice. Each lane was super-loaded with 34243 cells for a target of 17000 single cells per lane at a multiplet rate of 3%[97]. The stromal cell dataset used 4 lanes of a Chromium Next GEM Chip, with lane 1 containing *Il1r1*$^{-/-}$ stromal cells from *Mtb*-infected mice, lane 2 containing *Il1r1*$^{-/-}$ stromal cells from naïve mice, lane 3 containing wild-type stromal cells from *Mtb*-infected mice, and lane 4 containing wild-type stromal cells from naïve mice. Each lane was loaded with 12500 cells for an expected yield of 7000 single cells at a multiplet rate of 5%. The T cell and ILC libraries were generated using the same Chromium Next GEM Chip, with lane 1 containing T cells and lane 2 containing ILCs from *Mtb*-infected mixed BM chimera mice. 25000 cells were super-loaded into each lane with a target capture of 13200 cells at a multiplet rate of 4%[97]. For the CITE-seq libraries, 0.5 U/µL RNaseOUT Recombinant Ribonuclease Inhibitor (Invitrogen) was added to single cell RT master mix during the loading step and 1 µL of ADT and HTO additive primers (0.2 µM stock) were added during the cDNA amplification. All samples were decontaminated by 2 rounds of centrifugation through 0.2 µM filter microcentrifuge tubes following cDNA, ADT, and HTO purification and then removed from the BSL3. The CITE-seq protocol was used to complete the ADT and HTO libraries while the 10X Genomics protocol was followed for the cDNA library. Quality control of the libraries was performed with a Fragment Analyzer (Agilent). Libraries were pooled and then sequenced on a NovaSeq 6000 (Illumina) using an S1 flow cell and the following cycles read 1 (28 cycles), i7 index (10 cycles), i5 index (10 cycles), read 2 (90 cycles).

ScRNA-seq: data processing.

Sequencing reads of the mRNA libraries were mapped to the mouse genome with CellRanger version 6.0.0 (10X Genomics), while the raw count matrices for the ADT and HTO libraries were generated with CITE-Seq-Count version 1.4.3[98]. The count matrices were analyzed with Seurat v4.3.0[38] using default settings for normalizing the data, finding variable features, and scaling the data. For CITE-seq datasets, multiplets were excluded through HTO demultiplexing using the HTODemux function. The myeloid cell dataset was filtered to include cells with between 200

and 4500 genes and less than 5% mitochondrial reads. The T cell, ILC, and stromal cell datasets were filtered to only include cells that have between 200 and 2500 genes and less than 5% mitochondrial reads. The resulting myeloid dataset as well as our previously published scRNA-seq datasets for myeloid cells in *Mtb*-infected and naïve B6 and *Sp140*$^{-/-}$ mice (GSE216023) were integrated together and then clustered with a resolution of 1.5. The T cell and ILC datasets were analyzed with the default Seurat workflow using weighted nearest neighbor multimodal analysis to cluster cells based on mRNA and protein expression at a resolution of 1. The stromal cell dataset was also analyzed with Seurat using integration to combine the *Mtb*-infected and naïve WT and *Il1r1*$^{-/-}$ datasets and then clustering the cells based on mRNA expression using a resolution of 1.5.

Gene signature and ROC curve analysis

We previously published the type I IFN and IFNγ signatures used in this manuscript[17]. These signatures were applied to our myeloid cell scRNA-seq dataset to score cells based on their gene expression using the UCell package[99]. Signatures for the B6, *Nos2*$^{-/-}$, *Acod1*$^{-/-}$, and *Sp140*$^{-/-}$ mice were generated in R[100] by identifying genes induced at least 8-fold in the myeloid cells *Mtb*-infected mice relative to naïve animals for each genotype. The genes were converted from mouse to their human homolog using the convert_mouse_to_human_symbols from the NichetNetr package[56]. The hacksig package using the singscore statistical method[101] was applied to calculate a signature score based on each signature's expression in the TANDEM cohort PBMC RNA-seq data[43]. The pROC package[102] was used to generate the ROC curves and calculate the area under the curve to quantify the ability of each signature to discriminate between the active *Mtb* cases and healthy controls in the TANDEM cohort. The hacksig and pROC packages were also used to test the predictive ability of a gene signature consisting of known immunosuppressive genes (*IL1RN*, *IL18BP*, *CD274*, *TGFB1*, *IDO1*, *IL10*, and *ARG1*) on the TANDEM cohort. The pROC package was also used to determine the ability of IL1RN expression to identify active *Mtb* cases in the TANDEM cohort.

NicheNet analysis of IL-1-regulated signaling

IL-1-regulated genes were defined as genes expressed at least 2-fold higher in WT than *Il1r1*$^{-/-}$ cells in the T cell, innate lymphoid cell, and stromal cell scRNA-seq datasets. These IL-1-regulated genes were used as the potential ligands for NicheNet analysis[56]. The receiver cells were defined as IMs, Activated IMs, and *Spp1*$^{+}$ IMs from the myeloid cell scRNA-seq dataset. The expressed receptors on the receiver cells were identified using the get_expressed_genes function from NicheNet with a 10% cutoff for expression and then filtering the NicheNet receptor database to those genes expressed in the IM populations. Ligand activity in the receiver cells was calculated by identifying genes upregulated in Activated or *Spp1*$^{+}$ IMs relative to the IM cell population via the FindMarkers function from the Seurat package[38], focusing on genes upregulated at least 2-fold and with an adjusted p value less than 0.05, as calculated by the Wilcoxon Rank-Sum test with Bonferroni correction. Each IL-1-regulated ligand's ability to induce the genes upregulated in Activated or *Spp1*$^{+}$ IMs was determined by NicheNet's predict_ligand_activities function.

Statistical analysis

Statistical significance was determined using Prism (GraphPad) software for unpaired or paired two-tailed Student t test when comparing two populations, one-way ANOVA tests with Tukey's multiple comparisons test when comparing multiple groups. ROC curves and their AUC were calculated in R using the pROC package.

Data and code availability

Raw and processed single cell RNA-sequencing data is deposited at NCBI GEO. Code for scRNA-sequencing analysis is available on Github: https://github.com/dmitrikotov/.

Supplementary Figure Legends

Supplementary Figure 1. Classifying myeloid scRNA-seq clusters. Dot plot of lineage of markers used to (**a**) identify myeloid cell clusters and (**b**) define neutrophil cluster heterogeneity.

Supplementary Figure 2. Naïve *Sp140*-, *Nos2*-, and *Acod1*-deficient mouse lungs have few differentially expressed genes relative to naive B6 lungs. (**a**) The myeloid populations in the naïve lungs of B6, *Nos2*$^{-/-}$, *Acod1*$^{-/-}$, and *Sp140*$^{-/-}$ mice (n = 3 per genotype). (**b**) Number of shared and unique genes differentially expressed (2-fold change and adjusted p value < 0.05) between by neutrophils, alveolar macrophages, monocytes, and interstitial macrophages in *Nos2*$^{-/-}$, *Acod1*$^{-/-}$, and *Sp140*$^{-/-}$ relative to those from B6 mice. Statistical significance in (b) was calculated with the Wilcoxon Rank-Sum test with Bonferroni correction.

Supplementary Figure 3. Flow cytometric identification of monocyte and monocyte-derived macrophage subsets identified by scRNA-seq. (**a**) Overview of monocyte and interstitial macrophage subsets and (**b**) their expression of subset identifying markers. (**c**) Myeloid cell flow cytometry gating strategy. (**d**) Frequency of Mtb-infected cells among the major myeloid cell populations.

Supplementary Figure 4. IL-1Ra expression in mice and humans. (**a**) Myeloid cell expression of *Il1r2* and *Il1rn* in naïve and *Mtb*-infected lungs from B6, *Nos2*$^{-/-}$, *Acod1*$^{-/-}$, and *Sp140*$^{-/-}$ mice (n = 3 mice per genotype for naïve lungs and 3 mice per genotype for *Mtb*-infected lungs) as measured by scRNA-seq. (**b**) Normalized *IL1RN* expression in *Mtb*-infected (n = 151) and healthy individuals (n = 98) from the TANDEM cohort (analysis of GSE114192). (**c**) ROC curve of the predictive ability of an immunosuppressive gene signature applied to the TANDEM cohort.

Supplementary Figure 5. Myeloid cells express very little IL-1 receptor. (**a**) The myeloid populations identified by scRNA-seq and (**b**) *Il1r1* expression in myeloid cells from the lungs of B6, *Nos2*$^{-/-}$, *Acod1*$^{-/-}$, and *Sp140*$^{-/-}$ mice (n = 3 mice per genotype for naïve lungs and 3 mice per genotype for *Mtb*-infected lungs).

Supplementary Figure 6. Classifying T cell, ILC, and stromal cell scRNA-seq clusters. Dot plot of lineage of markers used to annotate the clusters in our (**a**) T cell dataset, (**b**) ILC dataset, and (**c**) stromal cell dataset.

Supplementary Figure 7. Neuronal IL-1 signaling does not impact *Mtb* control. (**a**) Experimental setup and (**b**) lung bacterial burden of bone marrow chimera mice with wild-type neurons (CD45.1 host, n = 13), littermate control neurons (Adv$^{+/+}$ Il1r1$^{fl/fl}$ host, n = 9), and IL-1 receptor-deficient neurons (Adv$^{Cre/+}$ Il1r1$^{fl/fl}$ host, n = 14) 25 days after *Mtb* infection. Pooled data from two independent experiments is shown in (B). Statistical significance in (B) was with a one-way ANOVA with Tukey's multiple comparison test.

Supplementary Figure 8. NicheNet analysis of IL-1 regulated ligands that could activate interstitial macrophages. (**a**) List of IL-1 regulated potential ligands identified in stromal and hematopoietic cells. (**b**) Receptor expression on interstitial macrophages for the IL-1-regulated ligands. (**c**) Predicted ligand activity based on genes differently expressed by the activated interstitial macrophage subsets.

Supplementary Table 1. Mouse gene signatures consisting of genes upregulated in myeloid cells following *Mtb* infection of B6, *Sp140*$^{-/-}$, *Acod1*$^{-/-}$, or *Nos2*$^{-/-}$ mice.

References

1. WHO. Global Tuberculosis Report 2022. https://www.who.int/teams/global-tuberculosis-programme/tb-reports/global-tuberculosis-report-2022 (2022).
2. Berry, M. P. R. *et al.* An interferon-inducible neutrophil-driven blood transcriptional signature in human tuberculosis. *Nature* **466**, 973–977 (2010).
3. Meier, S. *et al.* Neutrophil degranulation, NETosis and platelet degranulation pathway genes are co-induced in whole blood up to six months before tuberculosis diagnosis. *PLoS One* **17**, e0278295 (2022).
4. Zhang, G. *et al.* Allele-specific induction of IL-1β expression by C/EBPβ and PU.1 contributes to increased tuberculosis susceptibility. *PLoS Pathog* **10**, e1004426 (2014).
5. Mishra, B. B. *et al.* Nitric oxide controls the immunopathology of tuberculosis by inhibiting NLRP3 inflammasome-dependent processing of IL-1β. *Nat Immunol* **14**, 52–60 (2013).
6. Mishra, B. B. *et al.* Nitric oxide prevents a pathogen permissive granulocytic inflammation during tuberculosis. *Nat Microbiol* **2**, 17072 (2017).
7. Davenne, T. & McShane, H. Why don't we have an effective tuberculosis vaccine yet? *Expert Rev Vaccines* **15**, 1009–1013 (2016).
8. Cooper, A. M. *et al.* Disseminated tuberculosis in interferon gamma gene-disrupted mice. *J Exp Med* **178**, 2243–2247 (1993).

9. Flynn, J. L. *et al.* An essential role for interferon gamma in resistance to Mycobacterium tuberculosis infection. *J Exp Med* **178**, 2249–2254 (1993).

10. Flynn, J. L. *et al.* Tumor necrosis factor-alpha is required in the protective immune response against Mycobacterium tuberculosis in mice. *Immunity* **2**, 561–572 (1995).

11. Cohen, S. B., Gern, B. H. & Urdahl, K. B. The Tuberculous Granuloma and Preexisting Immunity. *Annual Review of Immunology* **40**, 589–614 (2022).

12. Russell, D. G., Barry, C. E. & Flynn, J. L. Tuberculosis: What We Don't Know Can, and Does, Hurt Us. *Science* **328**, 852–856 (2010).

13. McNab, F. W. *et al.* TPL-2-ERK1/2 signaling promotes host resistance against intracellular bacterial infection by negative regulation of type I IFN production. *J Immunol* **191**, 1732–1743 (2013).

14. Moreira-Teixeira, L. *et al.* T Cell-Derived IL-10 Impairs Host Resistance to Mycobacterium tuberculosis Infection. *J Immunol* **199**, 613–623 (2017).

15. Stanley, S. A., Johndrow, J. E., Manzanillo, P. & Cox, J. S. The Type I IFN response to infection with Mycobacterium tuberculosis requires ESX-1-mediated secretion and contributes to pathogenesis. *J Immunol* **178**, 3143–3152 (2007).

16. Ji, D. X. *et al.* Role of the transcriptional regulator SP140 in resistance to bacterial infections via repression of type I interferons. *eLife* **10**, e67290 (2021).

17. Kotov, D. I. *et al.* Early cellular mechanism of type I interferon-driven susceptibility to tuberculosis. 2022.10.06.511233 Preprint at https://doi.org/10.1101/2022.10.06.511233 (2023).

18. MacMicking, J. D. *et al.* Identification of nitric oxide synthase as a protective locus against tuberculosis. *Proc Natl Acad Sci U S A* **94**, 5243–5248 (1997).

19. Nair, S. *et al.* Irg1 expression in myeloid cells prevents immunopathology during M. tuberculosis infection. *Journal of Experimental Medicine* **215**, 1035–1045 (2018).

20. Moreira-Teixeira, L. *et al.* Type I IFN exacerbates disease in tuberculosis-susceptible mice by inducing neutrophil-mediated lung inflammation and NETosis. *Nat Commun* **11**, 5566 (2020).

21. Bohrer, A. C., Tocheny, C., Assmann, M., Ganusov, V. V. & Mayer-Barber, K. D. Cutting Edge: IL-1R1 Mediates Host Resistance to Mycobacterium tuberculosis by Trans-Protection of Infected Cells. *J Immunol* **201**, 1645–1650 (2018).

22. Eruslanov, E. B. *et al.* Neutrophil Responses to Mycobacterium tuberculosis Infection in Genetically Susceptible and Resistant Mice. *Infect Immun* **73**, 1744–1753 (2005).

23. Mattila, J. T., Maiello, P., Sun, T., Via, L. E. & Flynn, J. L. Granzyme B-expressing neutrophils correlate with bacterial load in granulomas from Mycobacterium tuberculosis-infected cynomolgus macaques. *Cell Microbiol* **17**, 1085–1097 (2015).

24. Gideon, H. P., Phuah, J., Junecko, B. A. & Mattila, J. T. Neutrophils express pro- and anti-inflammatory cytokines in granulomas from Mycobacterium tuberculosis-infected cynomolgus macaques. *Mucosal Immunol* **12**, 1370–1381 (2019).

25. Eum, S.-Y. *et al.* Neutrophils are the predominant infected phagocytic cells in the airways of patients with active pulmonary TB. *Chest* **137**, 122–128 (2010).

26. Lovewell, R. R., Baer, C. E., Mishra, B. B., Smith, C. M. & Sassetti, C. M. Granulocytes act as a niche for Mycobacterium tuberculosis growth. *Mucosal Immunol* **14**, 229–241 (2021).

27. Chowdhury, C. S. *et al.* Type I IFN signaling mediates NET release to promote Mycobacterium tuberculosis replication and granuloma caseation. 2022.11.29.518376 Preprint at https://doi.org/10.1101/2022.11.29.518376 (2022).

28. Ji, D. X. *et al.* Type I interferon-driven susceptibility to Mycobacterium tuberculosis is mediated by IL-1Ra. *Nat Microbiol* **4**, 2128–2135 (2019).

29. Law, K. *et al.* Increased release of interleukin-1 beta, interleukin-6, and tumor necrosis factor-alpha by bronchoalveolar cells lavaged from involved sites in pulmonary tuberculosis. *Am J Respir Crit Care Med* **153**, 799–804 (1996).

30. Mayer-Barber, K. D. *et al.* Host-directed therapy of tuberculosis based on interleukin-1 and type I interferon crosstalk. *Nature* **511**, 99–103 (2014).

31. Mayer-Barber, K. D. *et al.* Cutting Edge: Caspase-1 Independent IL-1β Production Is Critical for Host Resistance to Mycobacterium tuberculosis and Does Not Require TLR Signaling In Vivo. *J Immunol* **184**, 3326–3330 (2010).

32. Mayer-Barber, K. *et al.* Innate and adaptive interferons suppress IL-1α and IL-1β production by distinct pulmonary myeloid subsets during Mycobacterium tuberculosis infection. *Immunity* **35**, 1023–1034 (2011).

33. Di Paolo, N. C. *et al.* Interdependence between interleukin-1 and tumor necrosis factor controls TNF-dependent effector functions during Mycobacterium tuberculosis infection. *Immunity* **43**, 1125–1136 (2015).

34. Juffermans, N. P. *et al.* Interleukin-1 Signaling Is Essential for Host Defense during Murine Pulmonary Tuberculosis. *The Journal of Infectious Diseases* **182**, 902–908 (2000).

35. Kimmey, J. M. *et al.* Unique role for ATG5 in PMN-mediated immunopathology during M. tuberculosis infection. *Nature* **528**, 565–569 (2015).

36. Yeremeev, V., Linge, I., Kondratieva, T. & Apt, A. Neutrophils exacerbate tuberculosis infection in genetically susceptible mice. *Tuberculosis (Edinb)* **95**, 447–451 (2015).

37. Huynh, J. P. *et al.* Bhlhe40 is an essential repressor of IL-10 during Mycobacterium tuberculosis infection. *Journal of Experimental Medicine* **215**, 1823–1838 (2018).

38. Hao, Y. *et al.* Integrated analysis of multimodal single-cell data. *Cell* **184**, 3573-3587.e29 (2021).

39. Stoeckius, M. *et al.* Simultaneous epitope and transcriptome measurement in single cells. *Nat Methods* **14**, 865–868 (2017).

40. Marcovecchio, P. M., Thomas, G. & Salek-Ardakani, S. CXCL9-expressing tumor-associated macrophages: new players in the fight against cancer. *J Immunother Cancer* **9**, e002045 (2021).

41. Matsubara, E. *et al.* SPP1 Derived from Macrophages Is Associated with a Worse Clinical Course and Chemo-Resistance in Lung Adenocarcinoma. *Cancers (Basel)* **14**, 4374 (2022).

42. Bill, R. *et al.* CXCL9:SPP1 macrophage polarity identifies a network of cellular programs that control human cancers. *Science* **381**, 515–524 (2023).

43. Eckold, C. *et al.* Impact of Intermediate Hyperglycemia and Diabetes on Immune Dysfunction in Tuberculosis. *Clin Infect Dis* **72**, 69–78 (2020).

44. Mattila, J. T. *et al.* Microenvironments in tuberculous granulomas are delineated by distinct populations of macrophage subsets and expression of nitric oxide synthase and arginase isoforms. *J Immunol* **191**, 773–784 (2013).

45. Gopal, R. *et al.* S100A8/A9 proteins mediate neutrophilic inflammation and lung pathology during tuberculosis. *Am J Respir Crit Care Med* **188**, 1137–1146 (2013).

46. Gideon, H. P. *et al.* Multimodal profiling of lung granulomas in macaques reveals cellular correlates of tuberculosis control. *Immunity* **55**, 827-846.e10 (2022).

47. Zhou, T. *et al.* IL-18BP is a secreted immune checkpoint and barrier to IL-18 immunotherapy. *Nature* **583**, 609–614 (2020).

48. Jiang, X. *et al.* Role of the tumor microenvironment in PD-L1/PD-1-mediated tumor immune escape. *Molecular Cancer* **18**, 10 (2019).

49. Mittal, S. K., Cho, K.-J., Ishido, S. & Roche, P. A. Interleukin 10 (IL-10)-mediated Immunosuppression. *J Biol Chem* **290**, 27158–27167 (2015).

50. Gander-Bui, H. T. T. *et al.* Targeted removal of macrophage-secreted interleukin-1 receptor antagonist protects against lethal Candida albicans sepsis. *Immunity* **56**, 1743-1760.e9 (2023).

51. Scott, C. L. *et al.* The Transcription Factor ZEB2 Is Required to Maintain the Tissue-Specific Identities of Macrophages. *Immunity* **49**, 312-325.e5 (2018).

52. Lamacchia, C., Palmer, G., Seemayer, C. A., Talabot-Ayer, D. & Gabay, C. Enhanced Th1 and Th17 responses and arthritis severity in mice with a deficiency of myeloid cell–specific interleukin-1 receptor antagonist. *Arthritis & Rheumatism* **62**, 452–462 (2010).

53. Jain, A., Song, R., Wakeland, E. K. & Pasare, C. T cell-intrinsic IL-1R signaling licenses effector cytokine production by memory CD4 T cells. *Nat Commun* **9**, 3185 (2018).

54. Ohne, Y. *et al.* IL-1 is a critical regulator of group 2 innate lymphoid cell function and plasticity. *Nat Immunol* **17**, 646–655 (2016).

55. Zhou, L. *et al.* Innate lymphoid cells support regulatory T cells in the intestine through interleukin-2. *Nature* **568**, 405–409 (2019).

56. Browaeys, R., Saelens, W. & Saeys, Y. NicheNet: modeling intercellular communication by linking ligands to target genes. *Nat Methods* **17**, 159–162 (2020).

57. Mailhot, B. *et al.* Neuronal interleukin-1 receptors mediate pain in chronic inflammatory diseases. *J Exp Med* **217**, e20191430 (2020).

58. Liu, X. *et al.* Cell-Type-Specific Interleukin 1Receptor 1 Signaling in the Brain Regulates Distinct Neuroimmune Activities. *Immunity* **50**, 317-333.e6 (2019).

59. Hurskainen, M. *et al.* Single cell transcriptomic analysis of murine lung development on hyperoxia-induced damage. *Nat Commun* **12**, 1565 (2021).

60. Huang, L., Nazarova, E. V., Tan, S., Liu, Y. & Russell, D. G. Growth of Mycobacterium tuberculosis in vivo segregates with host macrophage metabolism and ontogeny. *Journal of Experimental Medicine* **215**, 1135–1152 (2018).

61. Ardain, A. *et al.* Group 3 innate lymphoid cells mediate early protective immunity against tuberculosis. *Nature* **570**, 528–532 (2019).

62. Gopal, R. *et al.* Unexpected Role for IL-17 in Protective Immunity against Hypervirulent Mycobacterium tuberculosis HN878 Infection. *PLOS Pathogens* **10**, e1004099 (2014).

63. Van Dis, E. *et al.* STING-Activating Adjuvants Elicit a Th17 Immune Response and Protect against Mycobacterium tuberculosis Infection. *Cell Rep* **23**, 1435–1447 (2018).

64. Jong, R. M. *et al.* Mucosal Vaccination with Cyclic Dinucleotide Adjuvants Induces Effective T Cell Homing and IL-17-Dependent Protection against Mycobacterium tuberculosis Infection. *J Immunol* **208**, 407–419 (2022).

65. Scriba, T. J. *et al.* Sequential inflammatory processes define human progression from M. tuberculosis infection to tuberculosis disease. *PLOS Pathogens* **13**, e1006687 (2017).

66. Coussens, L. M. & Werb, Z. Inflammation and cancer. *Nature* **420**, 860–867 (2002).

67. Ostrand-Rosenberg, S. & Sinha, P. Myeloid-Derived Suppressor Cells: Linking Inflammation and Cancer. *J Immunol* **182**, 4499–4506 (2009).

68. Huang, B. *et al.* Gr-1+CD115+ immature myeloid suppressor cells mediate the development of tumor-induced T regulatory cells and T-cell anergy in tumor-bearing host. *Cancer Res* **66**, 1123–1131 (2006).

69. Martinez, L. *et al.* Cytomegalovirus acquisition in infancy and the risk of tuberculosis disease in childhood: a longitudinal birth cohort study in Cape Town, South Africa. *The Lancet Global Health* **9**, e1740–e1749 (2021).

70. Müller, J. *et al.* Cytomegalovirus infection is a risk factor for tuberculosis disease in infants. *JCI Insight* **4**, 130090 (2019).

71. Walaza, S. *et al.* Influenza virus infection is associated with increased risk of death amongst patients hospitalized with confirmed pulmonary tuberculosis in South Africa, 2010–2011. *BMC Infectious Diseases* **15**, 26 (2015).

72. Antonelli, L. R. V. *et al.* Intranasal Poly-IC treatment exacerbates tuberculosis in mice through the pulmonary recruitment of a pathogen-permissive monocyte/macrophage population. *J Clin Invest* **120**, 1674–1682 (2010).

73. Kang, T. G. *et al.* Viral coinfection promotes tuberculosis immunopathogenesis by type I IFN signaling-dependent impediment of Th1 cell pulmonary influx. *Nat Commun* **13**, 3155 (2022).

74. Redford, P. S. *et al.* Influenza A Virus Impairs Control of Mycobacterium tuberculosis Coinfection Through a Type I Interferon Receptor–Dependent Pathway. *J Infect Dis* **209**, 270–274 (2014).

75. Volkert, M., Pierce, C., Horsfall, F. L. & Dubos, R. J. THE ENHANCING EFFECT OF CONCURRENT INFECTION WITH PNEUMOTROPIC VIRUSES ON PULMONARY TUBERCULOSIS IN MICE. *J Exp Med* **86**, 203–214 (1947).

76. Xu, W. *et al.* Early innate and adaptive immune perturbations determine long-term severity of chronic virus and Mycobacterium tuberculosis coinfection. *Immunity* **54**, 526-541.e7 (2021).

77. Ring, S. *et al.* Blocking IL-10 receptor signaling ameliorates Mycobacterium tuberculosis infection during influenza-induced exacerbation. *JCI Insight* **4**, e126533.

78. Dinarello, C. A. Overview of the IL-1 family in innate inflammation and acquired immunity. *Immunol Rev* **281**, 8–27 (2018).

79. McColl, S. R., Paquin, R., Ménard, C. & Beaulieu, A. D. Human neutrophils produce high levels of the interleukin 1 receptor antagonist in response to granulocyte/macrophage colony-stimulating factor and tumor necrosis factor alpha. *J Exp Med* **176**, 593–598 (1992).

80. Chensue, S. W., Warmington, K. S., Berger, A. E. & Tracey, D. E. Immunohistochemical demonstration of interleukin-1 receptor antagonist protein and interleukin-1 in human lymphoid tissue and granulomas. *Am J Pathol* **140**, 269–275 (1992).

81. Settas, L. D., Tsimirikas, G., Vosvotekas, G., Triantafyllidou, E. & Nicolaides, P. Reactivation of pulmonary tuberculosis in a patient with rheumatoid arthritis during treatment with IL-1 receptor antagonists (anakinra). *J Clin Rheumatol* **13**, 219–220 (2007).

82. Liu, X., Boyer, M. A., Holmgren, A. M. & Shin, S. Legionella-Infected Macrophages Engage the Alveolar Epithelium to Metabolically Reprogram Myeloid Cells and Promote Antibacterial Inflammation. *Cell Host Microbe* **28**, 683-698.e6 (2020).

83. Rothchild, A. C. *et al.* Role of Granulocyte-Macrophage Colony-Stimulating Factor Production by T Cells during Mycobacterium tuberculosis Infection. *mBio* **8**, 10.1128/mbio.01514-17 (2017).

84. Gonzalez-Juarrero, M. *et al.* Disruption of granulocyte macrophage-colony stimulating factor production in the lungs severely affects the ability of mice to control Mycobacterium tuberculosis infection. *J Leukoc Biol* **77**, 914–922 (2005).

85. Dis, E. V. *et al.* IFN-γ-independent control of M. tuberculosis requires CD4 T cell-derived GM-CSF and activation of HIF-1α. *PLOS Pathogens* **18**, e1010721 (2022).

86. Mayer-Barber, K. D. Granulocytes subsets and their divergent functions in host resistance to Mycobacterium tuberculosis - a 'tipping-point' model of disease exacerbation. *Curr Opin Immunol* **84**, 102365 (2023).

87. Müller, U. *et al.* Functional role of type I and type II interferons in antiviral defense. *Science* **264**, 1918–1921 (1994).

88. Shen, F. W. *et al.* Cloning of Ly-5 cDNA. *Proc Natl Acad Sci U S A* **82**, 7360–7363 (1985).

89. Glaccum, M. B. *et al.* Phenotypic and functional characterization of mice that lack the type I receptor for IL-1. *J Immunol* **159**, 3364–3371 (1997).

90. Robson, M. J. *et al.* Generation and Characterization of Mice Expressing a Conditional Allele of the Interleukin-1 Receptor Type 1. *PLoS One* **11**, e0150068 (2016).

91. Zhou, X. *et al.* Deletion of PIK3C3/Vps34 in sensory neurons causes rapid neurodegeneration by disrupting the endosomal but not the autophagic pathway. *Proc Natl Acad Sci U S A* **107**, 9424–9429 (2010).

92. Laubach, V. E., Shesely, E. G., Smithies, O. & Sherman, P. A. Mice lacking inducible nitric oxide synthase are not resistant to lipopolysaccharide-induced death. *Proc Natl Acad Sci U S A* **92**, 10688–10692 (1995).

93. Takaki, K., Davis, J. M., Winglee, K. & Ramakrishnan, L. Evaluation of the pathogenesis and treatment of Mycobacterium marinum infection in zebrafish. *Nat Protoc* **8**, 1114–1124 (2013).

94. Kotov, D. I., Pengo, T., Mitchell, J. S., Gastinger, M. J. & Jenkins, M. K. Chrysalis: A New Method for High-Throughput Histo-Cytometry Analysis of Images and Movies. *The Journal of Immunology* **202**, 300–308 (2019).

95. Gerner, M. Y., Kastenmuller, W., Ifrim, I., Kabat, J. & Germain, R. N. Histo-cytometry: a method for highly multiplex quantitative tissue imaging analysis applied to dendritic cell subset microanatomy in lymph nodes. *Immunity* **37**, 364–376 (2012).

96. Anderson, K. G. *et al.* Intravascular staining for discrimination of vascular and tissue leukocytes. *Nat Protoc* **9**, 209–222 (2014).

97. Stoeckius, M. *et al.* Cell Hashing with barcoded antibodies enables multiplexing and doublet detection for single cell genomics. *Genome Biology* **19**, 224 (2018).

98. Roelli, P., bbimber, Flynn, B., santiagorevale & Gui, G. Hoohm/CITE-seq-Count: 1.4.2. (2019) doi:10.5281/zenodo.2590196.

99. Andreatta, M. & Carmona, S. J. UCell: Robust and scalable single-cell gene signature scoring. *Comput Struct Biotechnol J* **19**, 3796–3798 (2021).

100. R Core Team. R: A language and environment for statistical computing. (2021).

101. Foroutan, M. *et al.* Single sample scoring of molecular phenotypes. *BMC Bioinformatics* **19**, 404 (2018).

102. Robin, X. *et al.* pROC: an open-source package for R and S+ to analyze and compare ROC curves. *BMC Bioinformatics* **12**, 77 (2011).

Figure 1. *Nos2*- and *Acod1*-deficient mice mimic human TB progression but do not exhibit type I interferon-driven *Mtb* susceptibility.

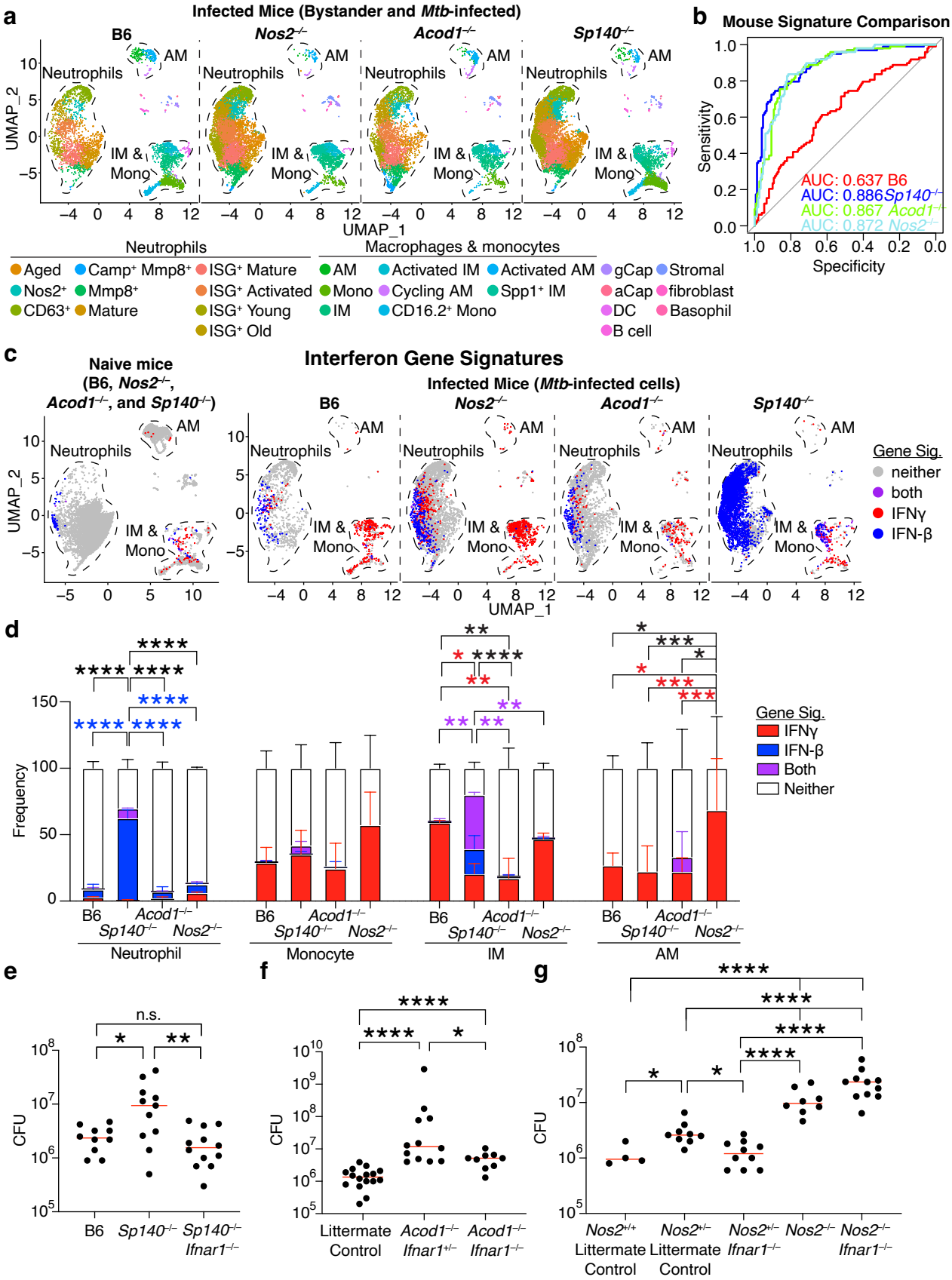

Supplementary Figure 1. Classifying myeloid cell scRNA-seq clusters.

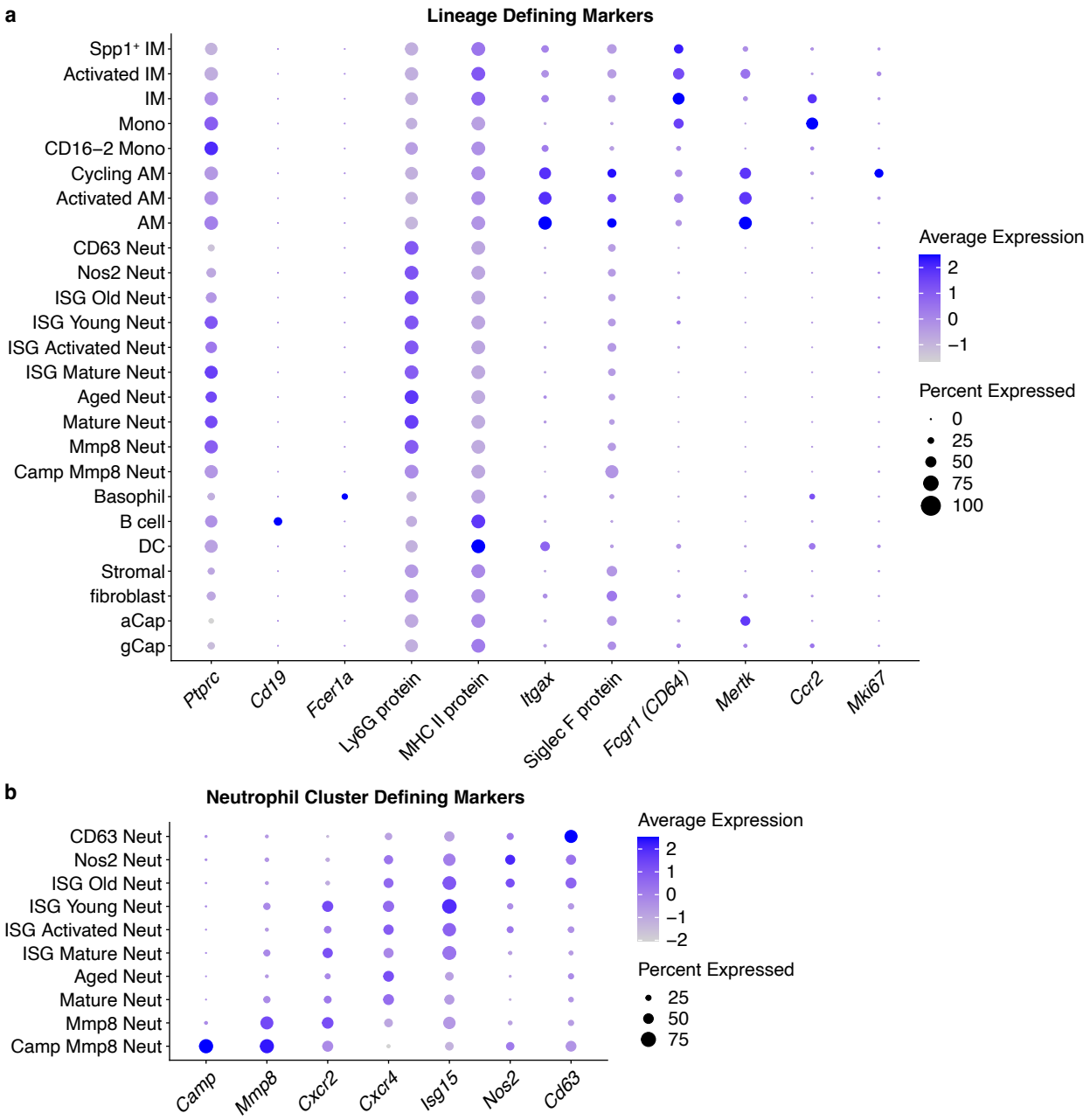

Supplementary Figure 2. Naive *Sp140*–, *Nos2*–, and *Acod1*–deficient mouse lungs have few differentially expressed genes relative to naive B6 lungs.

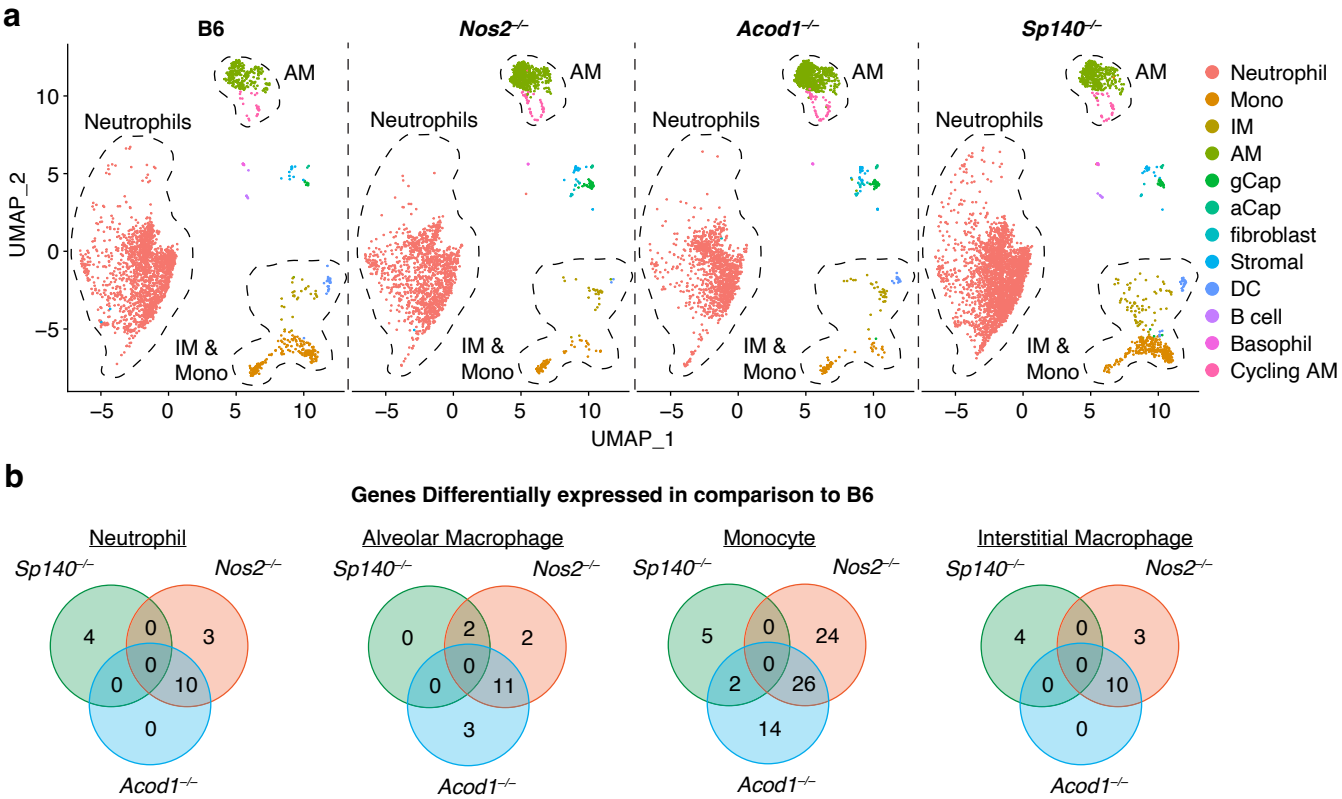

Supplementary Table 1

Gene	B6	*Sp140 −/−*	*Acod1 −/−*	*Nos2 −/−*
ARG1			X	X
ASPRV1			X	
ASS1			X	X
BATF2				X
CCL4		X	X	X
CCL5	X	X	X	X
CD38			X	
CD177			X	
CD274		X	X	X
CFB	X		X	X
CXCL9	X		X	X
CXCL10	X	X	X	X
GBP2	X	X	X	X
GBP4		X		X
GBP5	X	X	X	X
GBP6		X	X	X
GBP7				X
HERC6		X		
HLA-A	X	X		X
IFI16		X		
IFIT1B		X		
IFIT2		X	X	X
IFIT3		X		X
IL18BP		X	X	X
IL36G			X	
LCN2			X	
MMP14			X	
IL1A				X
INHBA		X		X
ISG15		X		
MIF				X
NOS2	X	X	X	X
OASL		X		
RSAD2		X		
SLAMF7		X		
USP18		X		
PARP14			X	
PLAC8			X	X
PSMB8				X
STAT1				X
UPP1			X	X
XAF1		X		X
ZBP1		X	X	X

Upregulated Genes

X

Immunosuppressive Genes

X

Figure 2. Neutrophils and interstitial macrophages localize to diseased tissue and are abundant, major expressors of IL-Ra.

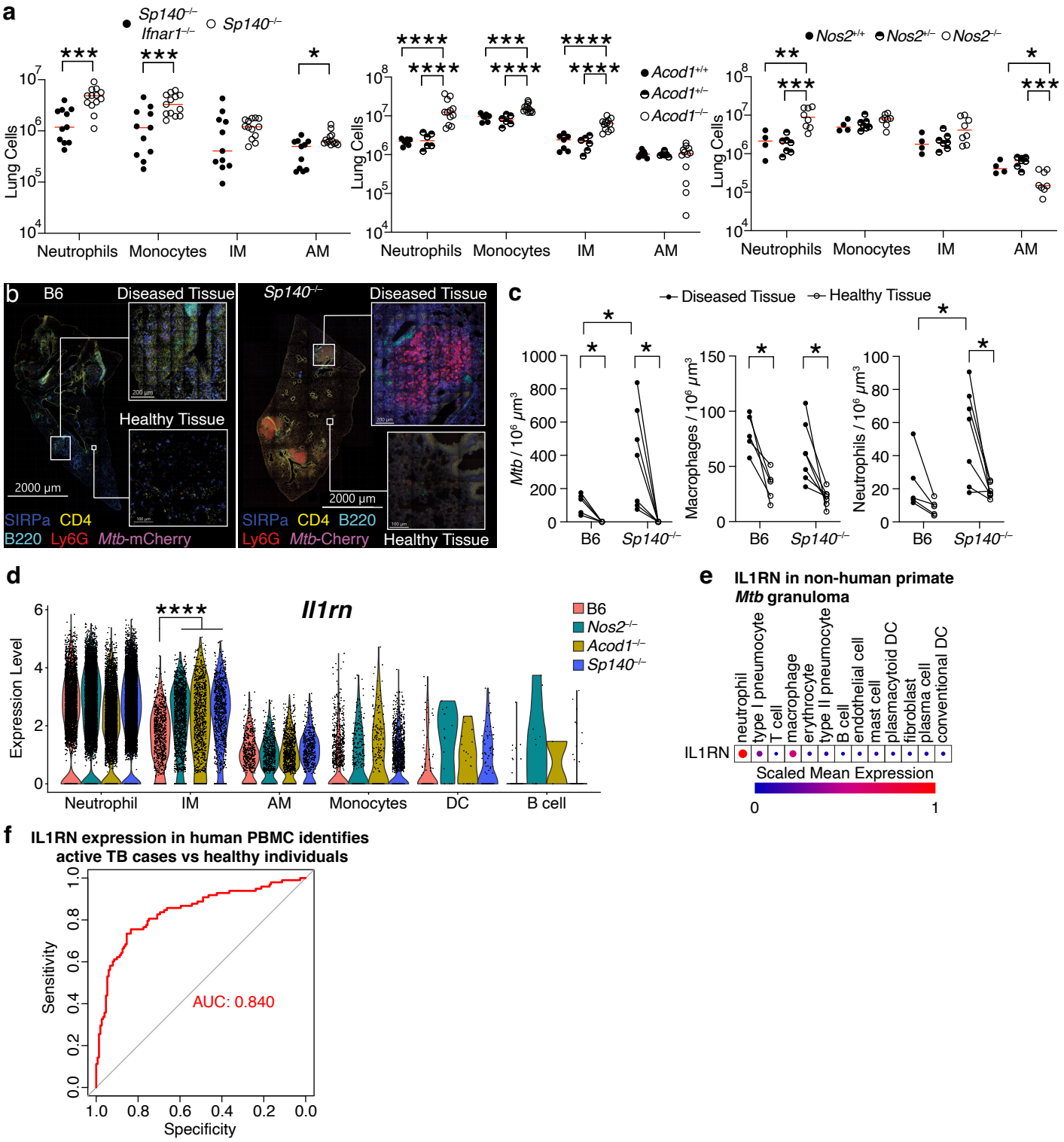

Supplementary Figure 3. Flow cytometric identification of monocyte and monocyte-derived macrophage subsets identified by scRNA-seq.

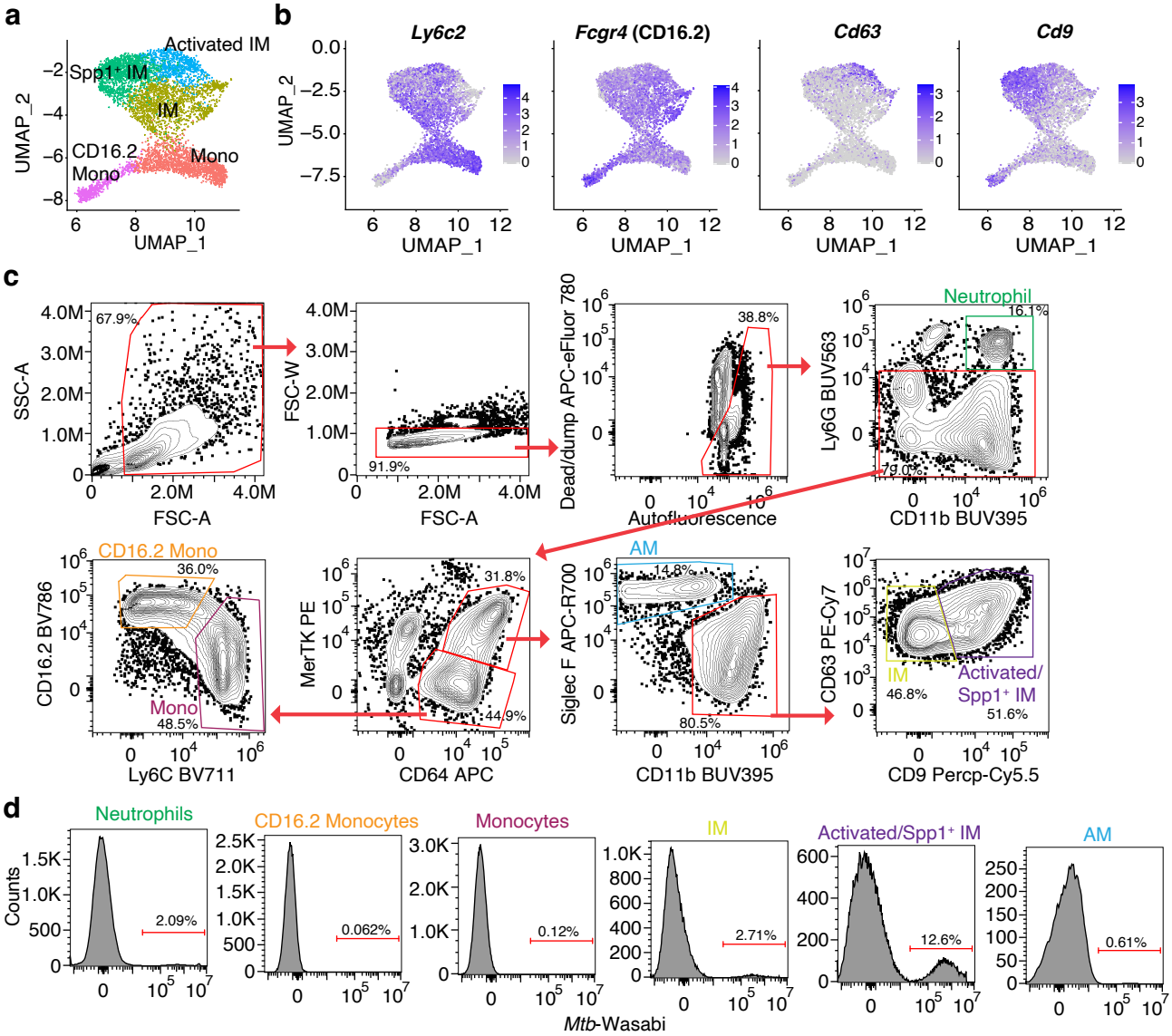

Supplementary Figure 4. IL-1Ra expression in mice and humans

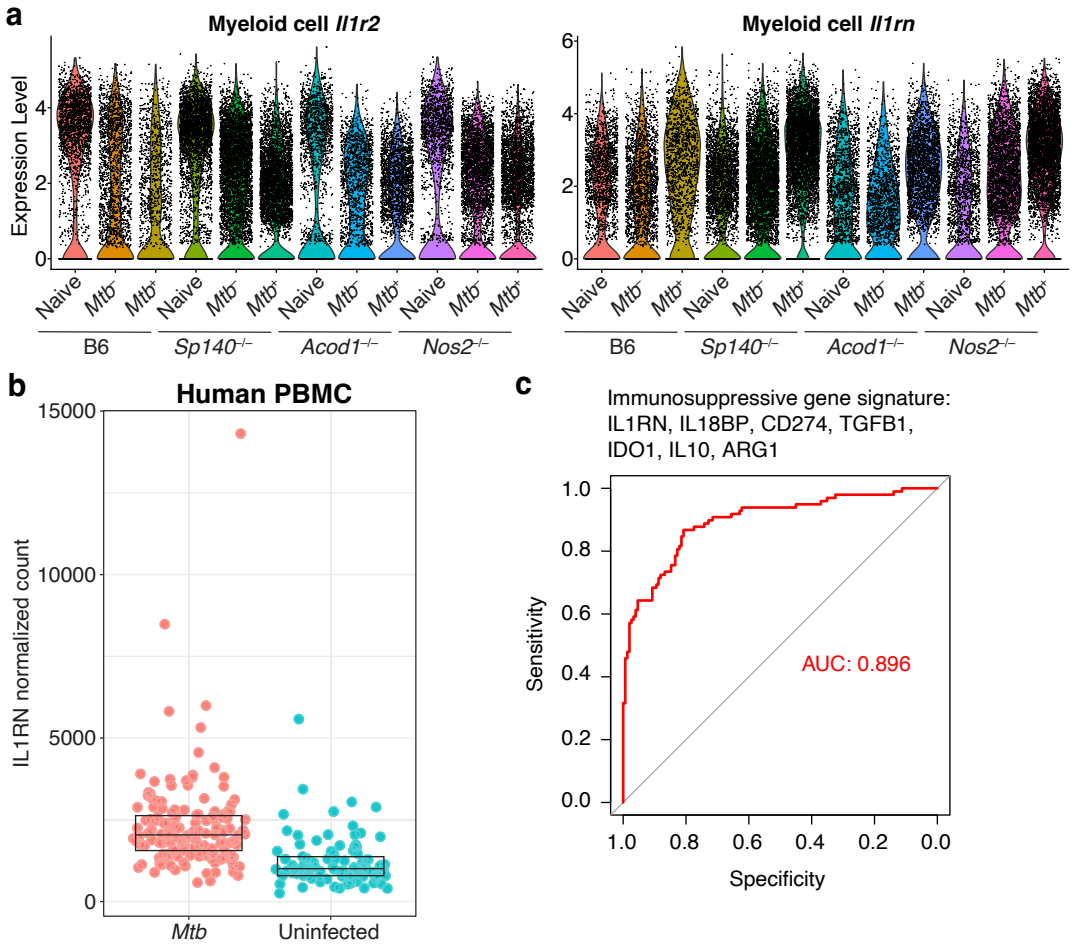

Figue 3. Macorphage-derived IL-1Ra is a conserved driver of *Mtb* susceptibility.

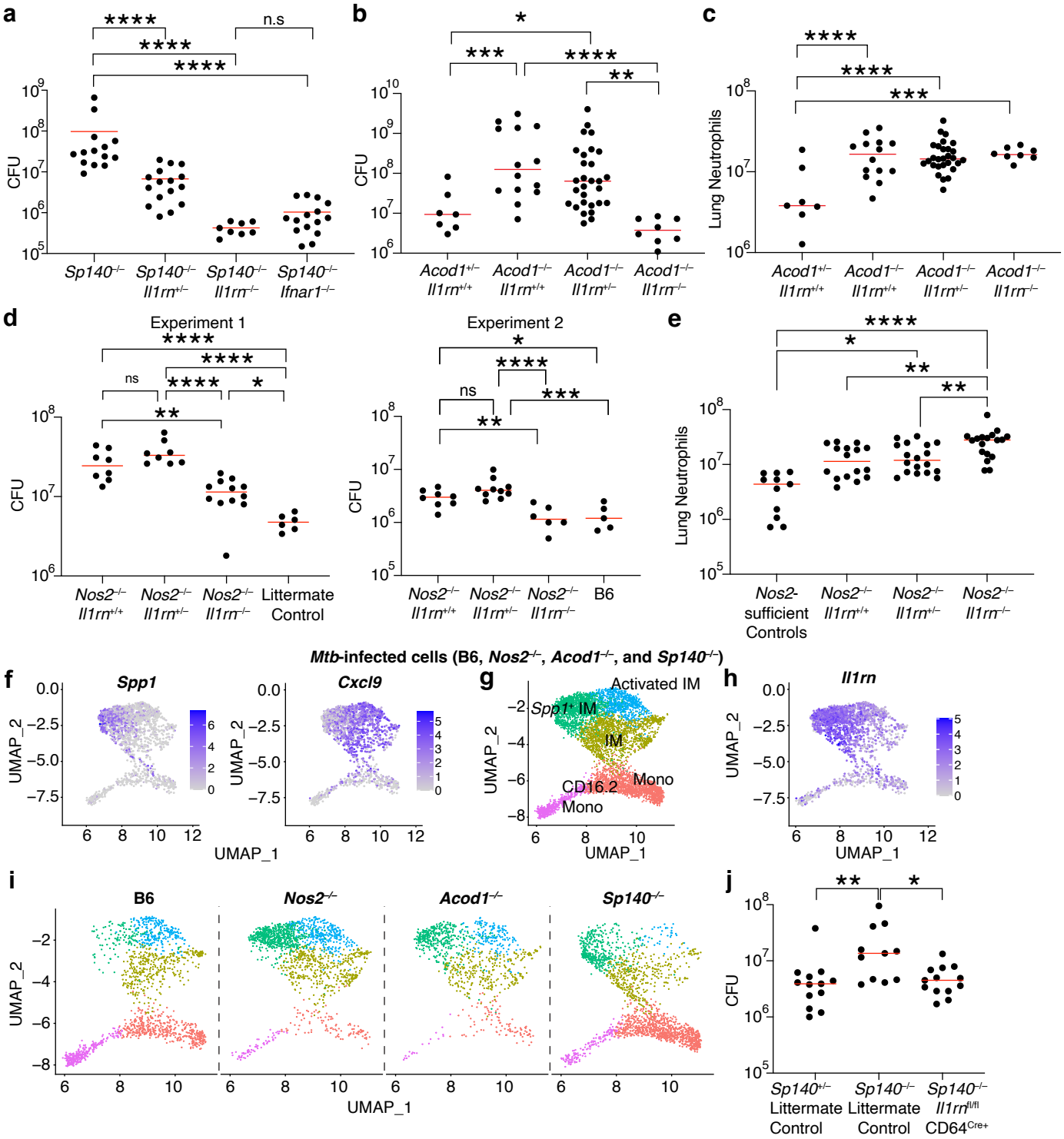

Figure 4. IL-1 enhances cytokine and chemokine expression by Th17, NKT17, and ILC3 as well as in stromal cells.

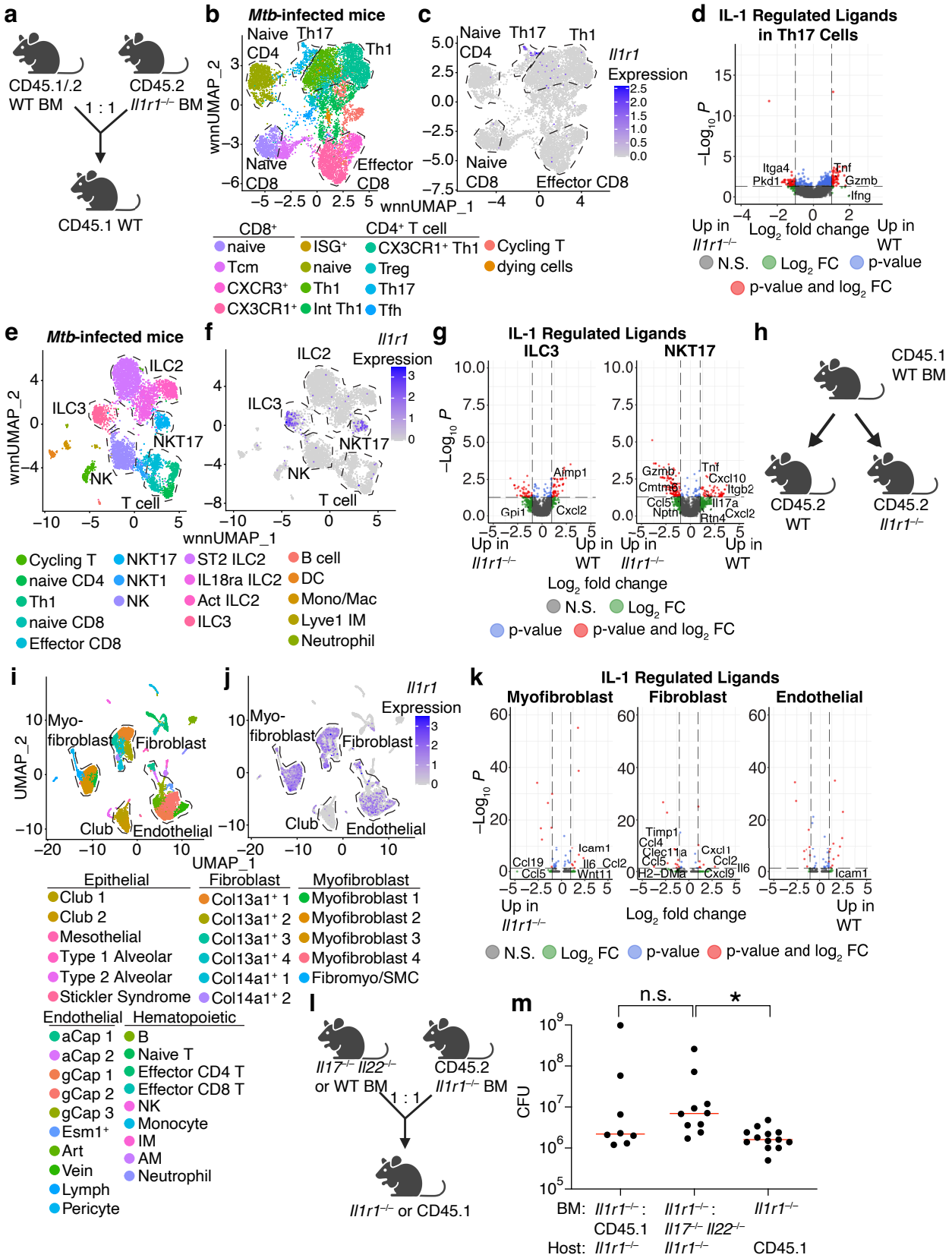

Supplementary Figure 5. Myeloid cells express very little IL-1 receptor.

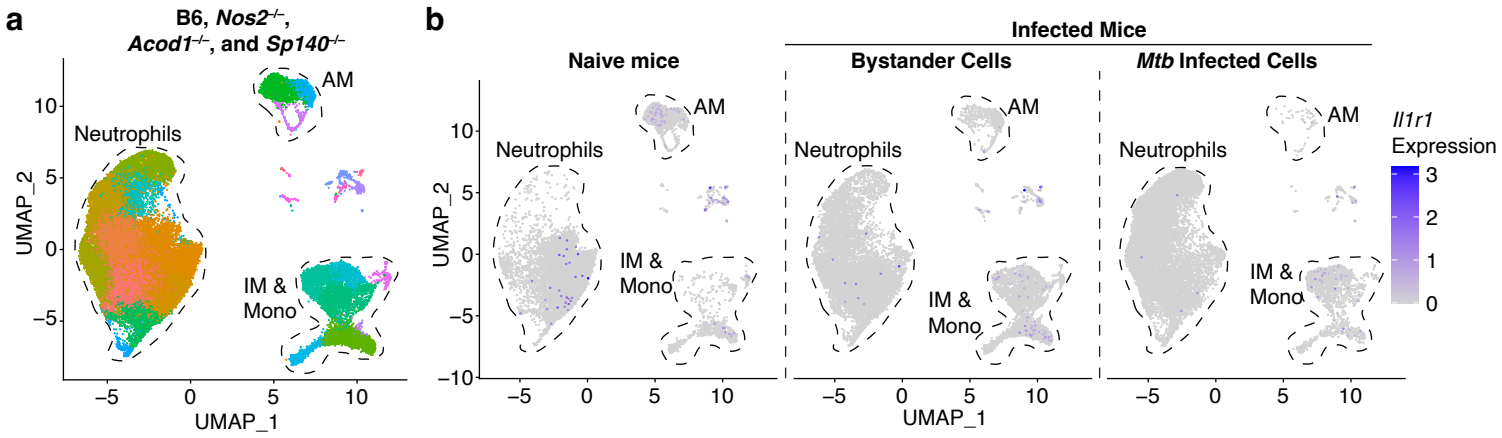

Supplementary Figure 6. Classifying T cell, ILC, and stromal cell scRNA-seq clusters.

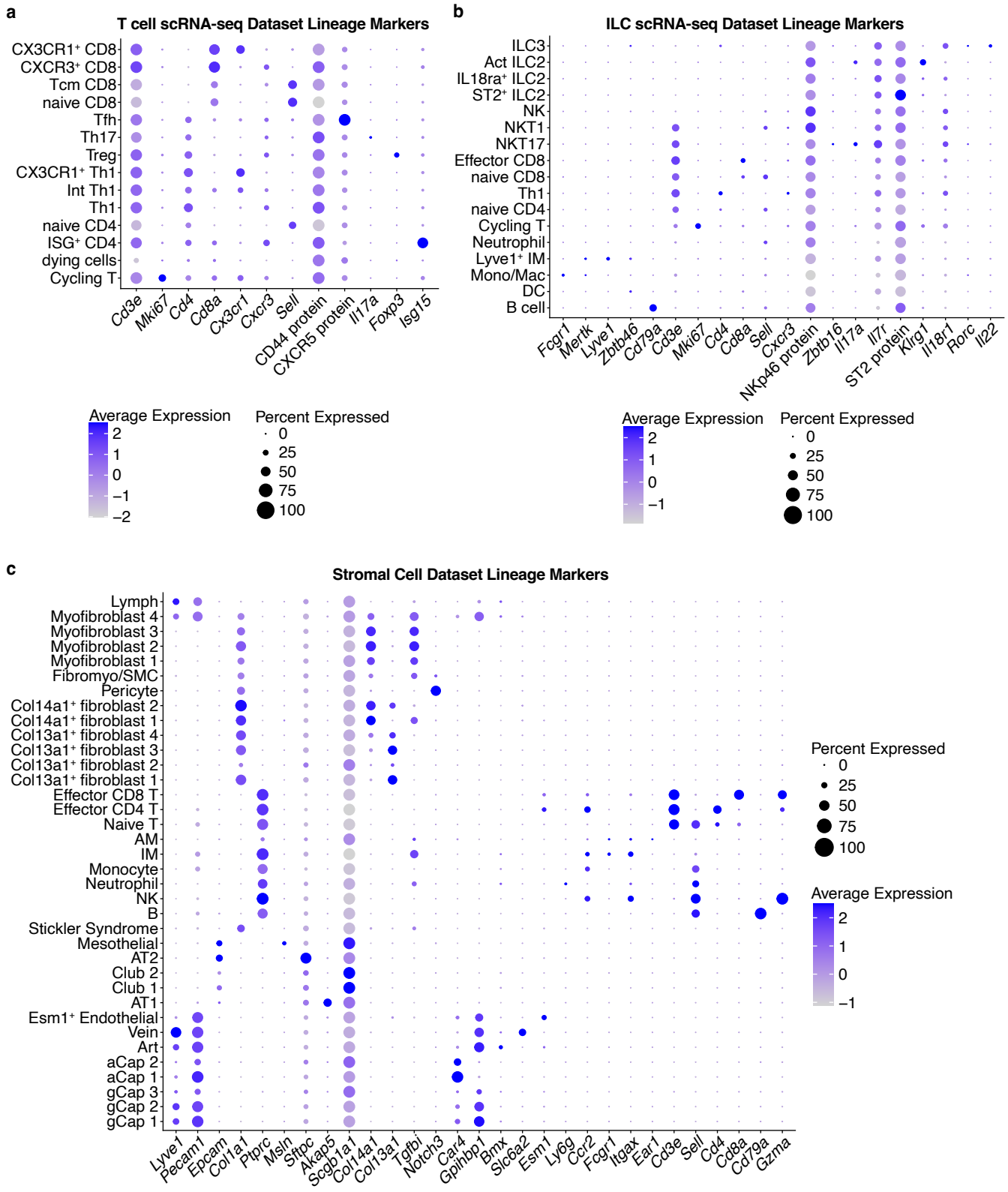

Supplementary Figure 7. Neuronal IL-1 signaling does not impact *Mtb* control.

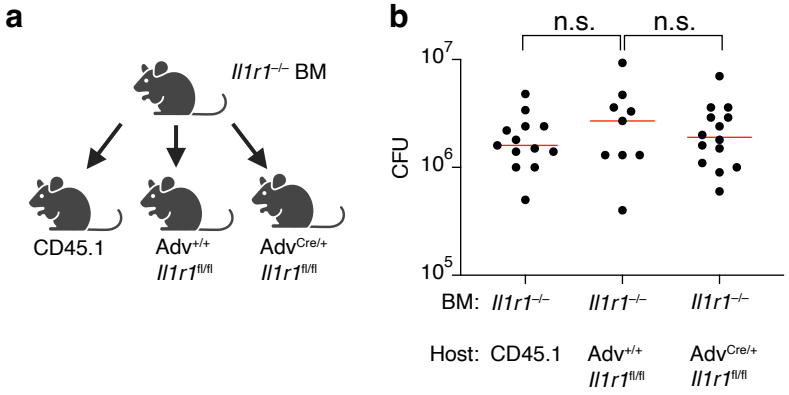
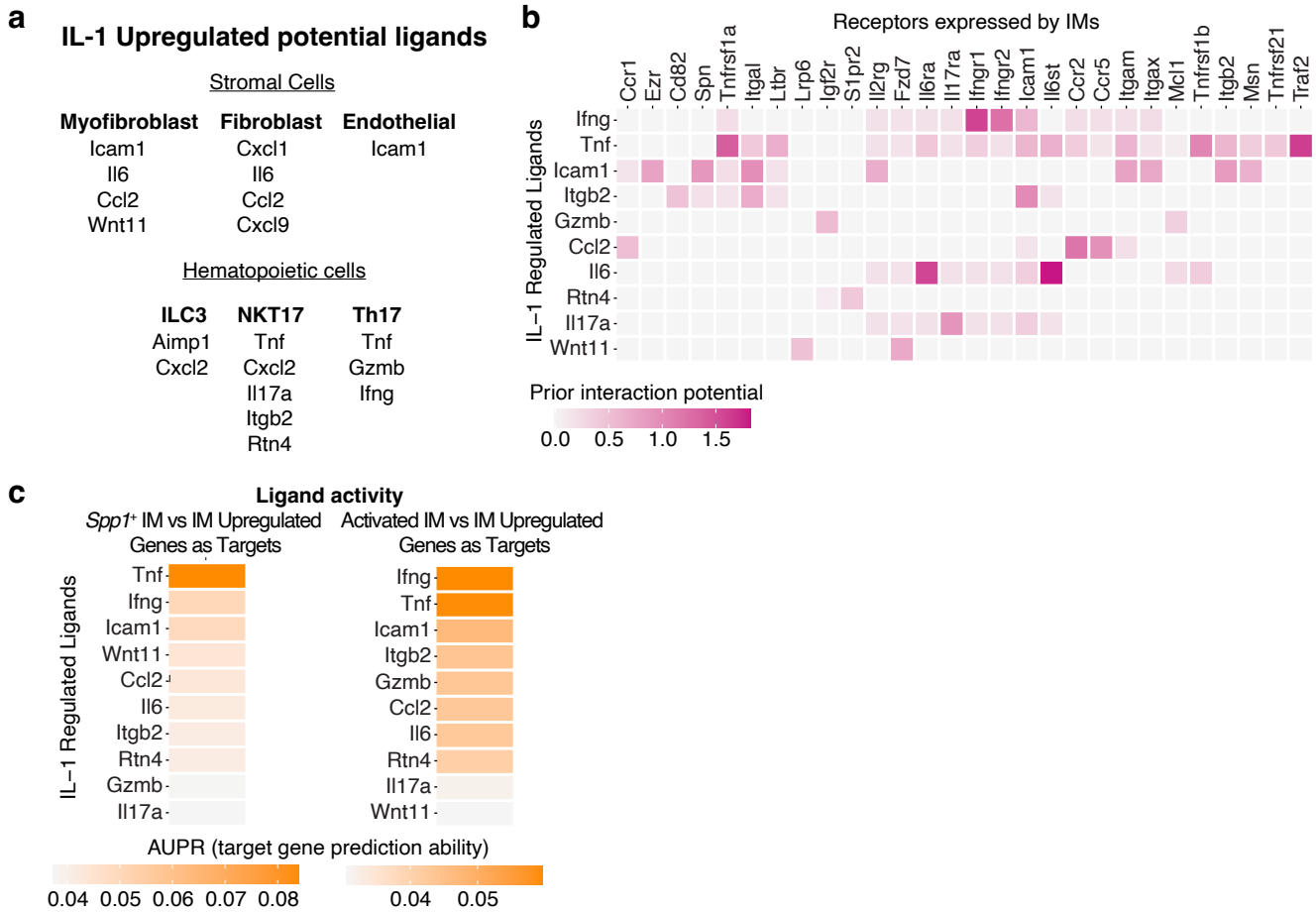
Supplementary Figure 8. NicheNet Analysis of IL-1 regulated ligands that could activate IMs.